HHS Public Access

Author manuscript

Mol Cell. Author manuscript; available in PMC 2022 June 17.

Published in final edited form as:

Mol Cell. 2021 June 17; 81(12): 2611–2624.e10. doi:10.1016/j.molcel.2021.03.034.

The Dystonia Gene THAP1 Controls DNA Double Strand Break Repair Choice

Kenta Shinoda[1], **Dali Zong**[1], **Elsa Callen**[1], **Wei Wu**[1], **Lavinia C. Dumitrache**[2], **Frida Belinky**[1], **Raj Chari**[3], **Nancy Wong**[1], **Momoko Ishikawa**[1], **Andre Stanlie**[1], **Trisha Multhaupt-Buell**[4], **Nutan Sharma**[4], **Laurie Ozelius**[4], **Michelle Ehrlich**[5], **Peter J. McKinnon**[2], **Andre Nussenzweig**[1,6,‡]

[1]Laboratory of Genome Integrity, National Cancer Institute, NIH, Bethesda, MD, USA

[2]St. Jude Translational Neuroscience, Center for Pediatric Neurological Disease Research, Depts. Genetics & Cell Mol. Biology, St. Jude Children's Research Hospital, Memphis, TN, USA

[3]Genome Modification Core, Frederick National Lab for Cancer Research, Frederick, MD, USA

[4]Department of Neurology, Massachusetts General Hospital and Harvard Medical School, Boston, MA, 02114, USA

[5]Department of Neurology, Icahn School of Medicine at Mount Sinai, New York, NY, USA

[6]Lead Contact

SUMMARY

The Shieldin complex shields double strand DNA breaks (DSBs) from nucleolytic resection. Curiously, the penultimate Shieldin component, SHLD1 is one of the least abundant mammalian proteins. Here, we report that the transcription factors THAP1, YY1 and HCF1 bind directly to the *SHLD1* promoter, where they cooperatively maintain the low basal expression of *SHLD1*, thereby ensuring a proper balance between end protection and resection during DSB repair. Loss of THAP1 dependent *SHLD1* expression confers cross resistance to PARP inhibitor and cisplatin in BRCA1-deficient cells, and shorter progression free survival in ovarian cancer patients. Moreover, the embryonic lethality and PARPi sensitivity of BRCA1 deficient mice is rescued by ablation of *SHLD1*. Our study uncovers a transcriptional network that directly controls DSB repair choice and suggests a potential link between DNA damage and pathogenic *THAP1* mutations, found in patients with the neurodevelopmental movement disorder adult-onset torsion dystonia type 6.

‡Correspondence: andre_nussenzweig@nih.gov.

Author Contributions

K.S., D.Z., E.C., and A.N. conceived and planned the study. K.S., D.Z., E.C., L.C.D., N.W., M.I., A.S. designed and performed experiments; K.S., D.Z., E.C., W.W. and F.B. analyzed the data; R.C. designed and generated *Shld1*$^{-/-}$ mice; T.M.-B., N.S., L.O., M.E., and P.J.M. supervised and provided advice; A.N. supervised the study. K.S., D.Z., and A.N. wrote the manuscript with comments from the authors.

Declaration of Interests

The authors declare no competing interests.

Graphical Abstract

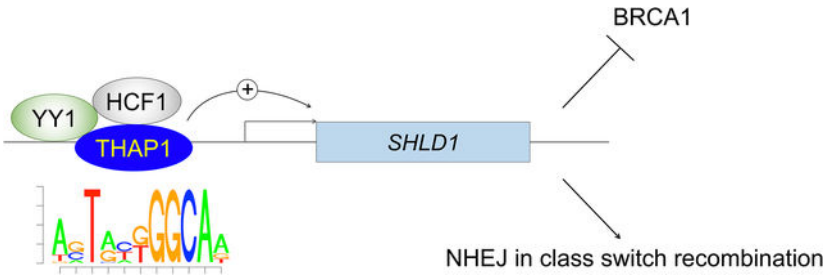

eTOC blurb:

The Shieldin complex inhibits homologous recombination by suppressing 5'−3' end resection and RAD51 loading. Shinoda et al demonstrate that physiological Shieldin activity is fine-tuned by THAP1-dependent transcription of the *SHLD1* gene. Dysregulation of THAP1 expression and/or function may therefore represent a new mechanism that modulates chemosensitivity in BRCA-deficient tumors.

INTRODUCTION

Direct joining of DNA double strand breaks (DSBs) by non-homologous end joining (NHEJ) provides eukaryotes with a fast and versatile mechanism for repairing genomic damage (Pannunzio et al., 2018). Although not as precise as homologous recombination (HR), NHEJ is essential for genome maintenance in non-dividing cells, which lack sister chromatids necessary for templating high fidelity HR. In addition, NHEJ supports physiological DNA rearrangement processes where genetic diversity is desirable, such as V(D)J recombination and immunogolobulin class switching (CSR) in developing lymphocytes (Rooney et al., 2004).

Once cells enter S-phase to commence DNA replication, HR gradually becomes an option as sister chromatids become available (Karanam et al., 2012). Extensive 5'-nucleolytic resection of DSBs is required to license HR, and is thought to simultaneously preclude NHEJ. The 3'-single-stranded (ss) overhang generated by resection is initially stabilized by RPA. The PALB2/BRCA2 mediator complex subsequently displaces RPA from the ssDNA and assembles polymers of the recombinase RAD51, which invade the intact sister chromatid to promote templated DNA synthesis (Zhao et al., 2019). HR is uniquely suitable for healing replication-associated DSBs, as most of them are one-ended. By contrast, NHEJ is either unable to repair such lesions or would give rise to translocations when disparate one-ended DSBs are inappropriately joined together. Consistently, deficiencies in HR not only facilitate tumorigenesis (Tarsounas and Sung, 2020), but also confer hypersensitivity to chemotherapeutic agents such as PARP inhibitors (PARPi) and cisplatin (Byrum et al., 2019) that challenge the replication fork.

53BP1 has emerged as a master regulator of DSB repair choice in mammalian cells (Mirman and de Lange, 2020; Setiaputra and Durocher, 2019). 53BP1 recruits a number of effector molecules, including PTIP (Callen et al., 2013), the Shieldin complex (consisting

of SHLD1, SHLD2, SHLD3 and REV7) (Boersma et al., 2015; Dev et al., 2018; Findlay et al., 2018; Gao et al., 2018; Ghezraoui et al., 2018; Gupta et al., 2018; Mirman et al., 2018; Noordermeer et al., 2018; Tomida et al., 2018; Xu et al., 2015), the CST complex (Barazas et al., 2018; Mirman et al., 2018) and DYNLL1 (He et al., 2018), to block DSB end resection. In addition, the 53BP1-RIF1-Shieldin subpathway is capable of directly impeding PALB2/BRCA2-mediated RAD51 loading on ssDNA (Callen et al., 2020). These barriers are normally overcome by the tumor suppressor BRCA1, which counteracts 53BP1 during S-phase by stimulating both nucleolytic resection and RAD51 assembly through still poorly defined mechanisms (Scully et al., 2019; Tarsounas and Sung, 2020). In addition to BRCA1, the AAA+ family ATPase TRIP13 promotes HR by catalyzing an inactivating conformational change in the REV7 component of the Shieldin complex (Clairmont et al., 2020).

Consistent with the antagonism between BRCA1 and 53BP1, much of the HR defects observed in BRCA1-deficient cells can be attributed to excessive 53BP1-mediated end-protection, which in turn promotes the toxic joining of replication-associated DSBs (Bouwman et al., 2010; Bunting et al., 2010; Callen et al., 2020; Jaspers et al., 2013). Notably, depletion of any Shieldin complex component restores HR in BRCA1-deficient cell lines (Dev et al., 2018; Gao et al., 2018; Ghezraoui et al., 2018; Gupta et al., 2018; Mirman et al., 2018; Noordermeer et al., 2018; Tomida et al., 2018), and reduced expression of Shieldin is associated with the acquisition of PARPi resistance in PDX models of BRCA1-deficient breast cancer (Dev et al., 2018).

These observations suggest that the level of Shieldin activity is a major determinant of HR competency and chemosensitivity in mammalian cells. Interestingly, Shieldin components are undetectable by mass spectrometry based proteome analysis (Gupta et al., 2018) and are amongst the lowest expressed genes (Ochs et al., 2019). Here, using a combination of CRISPR screens and biochemical assays, we addressed how changes in the levels of Shieldin affect DSB repair and genome stability. Our work reveals that the basal expression of *SHLD1* is maintained by direct binding of a network of transcription factors consisting of THAP1, HCF1 and YY1 to the *SHLD1* promoter. We find that inactivation of THAP1 abolishes *SHLD1* expression, leading to defective CSR, but HR restoration and chemoresistance in BRCA1-deficient cell lines. Conversely, overexpression of either SHLD1 or THAP1 compromises the repair of replication-associated DSBs in BRCA1-proficient cells, suggesting that maintaining low level SHLD1 expression is critical for genome stability.

RESULTS

Identification of THAP1 as a modifier of chemosensitivity in BRCA-deficient mouse models and human tumors

The Shieldin complex is recruited to DSBs by 53BP1 and RIF1 where it blocks HR by inhibiting nucleolytic end resection (Mirman and de Lange, 2020; Setiaputra and Durocher, 2019) as well as directly suppressing BRCA2-mediated loading of RAD51 recombinase onto ssDNA post-resection (Belotserkovskaya et al., 2020; Callen et al., 2020). These barriers to HR are normally overcome by BRCA1, but become insurmountable in

BRCA1-deficient cells and cause PARP inhibitor hypersensitivity. Here, we undertook whole-genome CRISPR-Cas9 screens to search for genes whose mutation confer PARPi resistance in BRCA1-deficient cells (Figure 1A). Human BRCA1-deficient tumors, particularly those that harbor pathogenic exon 11 mutations, often express a hypomorphic BRCA1 protein (BRCA1-Δ11q) (Wang et al., 2016). In order to model acquired PARPi resistance in a clinically relevant manner, we elected to use the PARPi-hypersensitive *Brca1*$^{\Delta 11}$ and *Brca1*$^{\Delta 11}$*Trp53bp1*^{S25A} murine models, in which a truncated BRCA1 protein (BRCA1-Δ11) highly similar to human BRCA1-Δ11q is expressed (Bunting et al., 2010; Callen et al., 2020; Wang et al., 2016). Moreover, cells derived from *Brca1*$^{\Delta 11}$ and *Brca1*$^{\Delta 11}$*Trp53bp1*^{S25A} mice exhibit marked HR defects due to excessive Shieldin-mediated end protection pre- and post-resection, respectively (Callen et al., 2020), thereby representing attractive murine model systems to search for putative regulators of Shieldin function.

Brca1$^{\Delta 11}$ and *Brca1*$^{\Delta 11}$*Trp53bp1*^{S25A} mouse embryonic fibroblasts (MEFs) expressing CAS9 were transduced with lentiviral libraries of single-guide RNAs (sgRNAs), and the resultant pools of edited cells were exposed to near-lethal doses of the clinically used PARPi olaparib for two weeks (Figure 1A). The screens were performed twice in *Brca1*$^{\Delta 11}$ MEFs and once in *Brca1*$^{\Delta 11}$*Trp53bp1*^{S25A} MEFs. Gene enrichment or depletion was calculated for each cell line using the MAGeCK algorithm (Li et al., 2014), with lower and higher RRA (Robust Rank Aggregation)-scores indicating positive and negative selection of a given gene deletion event, respectively (Figure 1B and Table S1). To obtain high-confidence hits, we combined the individual gene-based RRA-scores for both cell lines. Importantly, in both cell lines we identified multiple genes whose deletion have previously been shown to confer PARPi resistance in human BRCA1-deficient cells, including *Trp53bp1, Shld1*, *Shld2*, *Ctc1*, *Stn1* and *Dynll1* (Figure 1B and Table S1) (Dev et al., 2018; Findlay et al., 2018; Gao et al., 2018; Ghezraoui et al., 2018; Gupta et al., 2018; He et al., 2018; Mirman et al., 2018; Noordermeer et al., 2018; Tomida et al., 2018), thereby confirming the validity of our approach.

In addition, we identified *Thap1* as a candidate gene whose deletion strongly imparts PARPi resistance in both *Brca1*$^{\Delta 11}$ and *Brca1*$^{\Delta 11}$*Trp53bp1*^{S25A} MEFs (Figure 1B). *Thap1* encodes the murine homolog of Thanatos-associated protein 1 (THAP1), a transcription factor that is causatively linked to adult-onset torsion dystonia type 6 (DYT6) in humans, a neurodevelopmental disorder characterized by abnormal muscle contractions (Bressman et al., 2009; Djarmati et al., 2009; Fuchs et al., 2009). To verify the results of the primary screens, we conducted competitive growth assays using sgRNAs targeting either *Thap1* or *Trp53bp1* and found that each led to the outgrowth of two independently-derived *Brca1*$^{\Delta 11}$ MEF cell lines (14223 and S12) treated with PARPi (Figure 1C), while no difference in growth was observed without the drug (Figure S1A). In addition, we generated two independent clonal knockouts of *Thap1* using different sgRNAs in one of the two *Brca1*$^{\Delta 11}$ MEF cell lines (14223) (Figure S1B) and confirmed that deletion of *Thap1* led to cross-resistance to PARPi and cisplatin, as measured by cell viability assays and mitotic chromosome aberrations (Figures 1D, 1E, and S1C). Deletion of *THAP1* in two-independently derived clones of *BRCA1*-null human RPE1 cells (Noordermeer et al., 2018) likewise resulted in marked PARPi resistance (Figures 1F and S1D). Finally, we found that

low expression of *THAP1* was significantly correlated with shorter progression-free survival (PFS) of patients with *BRCA1*-mutated serous ovarian carcinoma (Figure 1G).

In contrast to BRCA1 deficiency, *Thap1* deletion did not affect the PARPi sensitivity of BRCA1-proficient cells as measured by cell viability (Figures S1E, S1F). Similarly, although most patients in this cohort have undergone platinum-based chemotherapy (Cancer Genome Atlas Research, 2011), no correlation with PFS was observed for patients with *BRCA1*-proficient tumors (Figure S1G). Altogether, these results support THAP1 as a *bona fide* modifier of chemosensitivity in BRCA1-deficient cells and tumors, and this effect is not species-, cell lineage- or *BRCA1* mutation-specific.

Intriguingly, a recent study of prognostic biomarkers of acute myelogenous leukemia reported that low levels of *BRCA2* and *THAP1* correlated with improved patient survival (Wang et al., 2020). Since BRCA1 and BRCA2 have functionally non-redundant roles during HR, we also sought to determine how *THAP1* expression influences the response of BRCA2-deficient cells to chemotherapy. In contrast to its impact on BRCA1-deficiency (Figures 1C–G), we found that deletion of *Thap1* increased genome instability in $Brca2^{Y3308X}$ mutant mouse embryonic stem cells (mESCs) treated with PARPi (Figure S1H). Consistent with increased therapeutic vulnerability, clinical data demonstrated that low *THAP1* expression was correlated with longer PFS in patients with *BRCA2*-mutant serous ovarian carcinoma (Figure S1I). Thus, THAP1 modulates the responses to chemotherapy in opposite ways in BRCA1- and BRCA2-deficient cells (see discussion).

THAP1 is a direct transcriptional regulator of *Shld1* expression

THAP1 has been proposed to regulate numerous target genes in neurons (Cheng et al., 2020; Frederick et al., 2019; Zakirova et al., 2018), but a potential link to DNA repair has not been described. While several transcription factors are thought to act directly at sites of DNA damage in a transcription-independent manner (Malewicz and Perlmann, 2014), we failed to observe THAP1 relocalization to sites of DNA damage induced by γ-irradiation (not shown). Given that most of the dystonia-causing mutations in THAP1 disrupt its sequence-specific DNA binding activity (Blanchard et al., 2011; Charlesworth et al., 2013), we hypothesized that THAP1 may regulate the chemosensitivity of BRCA-deficient cells directly through transcriptional mechanisms.

To investigate this possibility, we performed nascent RNA-sequencing (RNA-seq) to systematically probe for genes that are differentially expressed in $Thap1^{-/-}$ and $Thap1^{-/-}$ $Brca1^{\Delta 11}$ MEFs, as compared to wild-type and $Brca1^{\Delta 11}$ parental cells, respectively. In total, we found 452 differentially expressed genes (221 downregulated and 231 upregulated (log2 fold-change >2 and FDR <0.05) between $Thap1^{-/-}$ and wild-type cells, while 1,337 genes were differentially expressed (675 downregulated and 662 upregulated) between $Thap1^{-/-}Brca1^{\Delta 11}$ and $Brca1^{\Delta 11}$ cells (Figure 2A). Of these, 98 genes (57 downregulated and 41 upregulated) were common to both $Thap1^{-/-}$ and $Thap1^{-/-}Brca1^{\Delta 11}$ cells (Table S2). We chose to examine this set of common genes so as to minimize spurious findings due to non-isogenic cellular backgrounds. To determine which of these genes are direct targets of THAP1, we performed THAP1 ChIP-sequencing (ChIP-seq) in MEFs which identified 2,134 unique THAP1 binding sites (Figure 2A). Overall, only six differentially expressed

genes in *Thap1*-deficient MEFs were also bound by THAP1 (Figure 2B). Among these genes we identified *Shld1*, the penultimate component of the Shieldin complex and a known effector of 53BP1. Re-examining our RNA-seq datasets, we confirmed that *Shld1* expression was significantly decreased in *Thap1*$^{-/-}$ and *Thap1*$^{-/-}$ *BRCA1*$^{\Delta 11/\Delta 11}$ MEFs (Figure 2C). By contrast, genes encoding 53BP1 pathway members including *Shld2*, *Shld3* and *Rev7* exhibited only modest expression changes (Figures S2A and S2B).

Sequence-specific DNA binding of THAP1 is mediated by the THAP-type zinc finger located within its THAP domain and is disrupted by the C54Y point mutation, a known DYT6 causative mutation (Roussigne et al., 2003; Ruiz et al., 2015). To determine whether THAP1 DNA binding is required for *Shld1* expression, we re-analyzed a RNA-seq dataset derived from *Thap1*$^{C54Y/C54Y}$ mESCs (Aguilo et al., 2017). We found that *Shld1* expression was decreased in *Thap1*$^{C54Y/C54Y}$ cells at a level comparable to that found in *THAP1*$^{-/-}$ mESCs (Figures 2D and S2C). Thus, sequence-specific DNA binding is required for THAP1 regulation of SHLD1.

The *Shld1* promoter contains a consensus THAP1 binding sequence (THABS) motifs where a strong THAP1 ChIP-seq signal was detected (Figure 2E) (Clouaire et al., 2005). To verify that the integrity of THABS is important for THAP1-driven *Shld1* expression, we deleted the THABS motif in *BRCA1*$^{\Delta 11/\Delta 11}$ MEFs by CRISPR-Cas9 gene editing (Figure 2F). We found that deletion of THABS from the *Shld1* promoter phenocopied *Thap1* deletion and led to PARPi resistance in *BRCA1*-deficient cells as measured by cell viability assays (Figure 2G). Thus, THAP1 binding to *Shld1* promoter is required for its ability to modulate chemosensitivity in *BRCA1*$^{\Delta 11/\Delta 11}$ MEFs.

A THAP1-HCF1-YY1 co-regulatory module promotes *Shld1* expression

Recent studies have shown that THAP1 frequently co-occupy its target genes with the transcriptional co-regulators HCF1 and YY1 (Mazars et al., 2010; Michaud et al., 2013; Yellajoshyula et al., 2017), which are recruited to the promoters by THAP1 (Hollstein et al., 2017; Yellajoshyula et al., 2017). Analyses of ChIP-seq datasets revealed that HCF1 and YY1 indeed co-occupy the *Shld1* promoter with THAP1 both in mouse (Figure 2H) and in human (Figure S2D). Moreover, we found that inducible deletion of *Hcfc1* in hepatocytes (*Hcfc1*$^{HepKO/Y}$) led to downregulation of *Shld1* expression (Figure S2E) (Minocha et al., 2019). Similarly, conditional knockout of *Yy1* in mouse B cells (*Yy1*$^{flox/flox}$ TAT-Cre) significantly decreased *Shld1* expression (Figure S2F) (Nandi et al., 2020b). Strikingly, when we overlapped genes whose expression were differentially regulated by HCF1, YY1 and THAP1 and that were also direct targets of these transcription factors, only two genes *Shld1* and *Gm11520* (a putative noncoding RNA of unknown function) showed significant enrichment (Figures 2I, S2G and S2H). Thus, although the vast majority of genes appear to be independently regulated by THAP1, HCF1 and YY1, these cofactors cooperatively bind to the *Shld1* promoter to maintain its expression.

Imbalances in the THAP1-SHLD1 axis threaten genome stability

SHLD1 was recently shown to be amongst the lowest expressed genes in the mammalian proteome (Gupta et al., 2018; Ochs et al., 2016). This prompted us to investigated whether

elevating SHLD1 protein levels cause cellular toxicity. To this end, we overexpressed exogenous SHLD1 or THAP1 in BRCA1-proficient MEFs (Figure 3A). We found that overexpression of SHLD1 and to a lesser extent THAP1 significantly potentiated PARPi-induced genomic instability (Figures 3B and S3A). Importantly, deleting SHLD1 completely abrogated THAP1 overexpression-induced genome instability (Figures 3C and S3B). We also found that THAP1 overexpression increased endogenous *Shld1* expression, which in turn appeared to provide a negative feedback on THAP1 transcription activity (Figure S3C). Altogether, these results are consistent with the notion that excessive expression of SHLD1 can impair genome integrity even in WT cells, which explains why its expression must be fine-tuned by THAP1-mediated transcriptional regulation. Interestingly, analysis of publicly available gene expression databases revealed that, while *THAP1* is ubiquitously expressed in malignant tissues, its expression is notably increased in testis, ovarian and breast cancers (Figure 3D), suggesting that dysregulation of *THAP1* could potentially impact tumorigenesis and responses to therapy.

THAP1 inhibits DNA end resection and RAD51 nucleofilament formation

The precise function of SHLD1 within the 53BP1 pathway is unknown. Previous studies have implicated SHLD3 as the anchor that attaches the entire Shieldin complex to RIF1, enabling its recruitment to 53BP1-decorated chromatin (Dai et al., 2020; Noordermeer et al., 2018; Setiaputra and Durocher, 2019). We therefore tested whether THAP1 loss would impact the recruitment of 53BP1, RIF1 and SHLD3 to sites of DNA damage. We found that foci formation for 53BP1, RIF1, and SHLD3 was not impaired in $Thap1^{-/-}Brca1^{\Delta 11}$ cells but rather, was somewhat enhanced (Figures S4A–S4C). In BRCA1-deficient cells, unmitigated activation of the 53BP1-RIF1-Shieldin pathway impairs HR by blocking DSB end-resection and RAD51 nucleofilament formation (Dev et al., 2018; Findlay et al., 2018; Gao et al., 2018; Ghezraoui et al., 2018; Gupta et al., 2018; He et al., 2018; Mirman et al., 2018; Noordermeer et al., 2018; Tomida et al., 2018). Indeed, we found that deletion of *Thap1* rescued both irradiation-induced RPA foci and RAD51 nucleofilament formation in $Brca1^{\Delta 11}$ MEFs to wild-type levels (Figures 4A, 4B, S4D and S4E). Moreover, $Thap1^{-/-}Brca1^{\Delta 11}$ MEFs exhibited normal HR capacity when assayed with a recombination reporter (Kuhar et al., 2014), whereas parental $Brca1^{\Delta 11}$ cells were clearly HR deficient (Figure 4C). Thus, loss of THAP1 promotes end-resection and HR proficiency in BRCA1-deficient cells, which may explain why doubly deficient cells acquire resistance to PARPi and cisplatin.

Given the apparent importance of THAP1 in promoting 53BP1-Shieldin function, we surmised that ablation of *Thap1* might rescue genome instability and embryonic lethality seen in BRCA1-deficient mice. A direct test of this hypothesis is not possible, however, as *Thap1* is an essential gene in mice (Ruiz et al., 2015). Instead, we generated *Shld1* knockout mice (Figure S5A). *Shld1* knockout mice were viable and did not display any overt phenotypes (Figure 4D). Nevertheless, $Shld1^{-/-}$ mice showed defects in class switch recombination (CSR) similar to $Trp53b1^{-/-}$(Figure S5B). Moreover, when we crossed $Shld1^{-/-}$ with $Brca1^{\Delta 11/+}$ mice, we found that $Shld1^{-/-}Brca1^{\Delta 11}$ mice were obtained at the expected Mendelian ratio, similar to *Trp53b1 deficiency* (Figure 4D). Finally, PARPi-induced genome instability was significantly lower in primary $Shld1^{-/-}Brca1^{\Delta 11}$ B cells

compared to similarly treated *Brca1*$^{\Delta 11}$ counterparts (Figures S5C and S5D). Altogether, these data provide a clear mechanistic basis to explain how perturbations in the THAP1-SHLD1 axis impacts BRCA1 deficiency. Furthermore, the fact that a deficiency in Shieldin components (Ling et al., 2020) or 53BP1 itself, but not other 53BP1 pathway members (such as PTIP, RIF1, TRIP13), could rescue the embryonic lethality of *Brca1*$^{\Delta 11}$ mice fully support Shieldin as the ultimate 53BP1 effector of DSB choice.

To provide definitive proof that the observed PARPi resistance in *Thap1*$^{-/-}$*Brca1*$^{\Delta 11}$ MEFs was due to decreased *Shld1* expression, we re-introduced SHLD1 in *Thap1*$^{-/-}$*Brca1*$^{\Delta 11}$ MEFs (Figure 4E). Ectopic expression of SHLD1 in *Thap1*$^{-/-}$*Brca1*$^{\Delta 11}$ MEFs restored their hypersensitivity to PARPi (Figure 4F). As expected, add-back of THAP1 in *Thap1*$^{-/-}$*Brca1*$^{\Delta 11}$ MEFs also restored PARPi hypersensitivity (Figures 4E and 4F), while a THAP1 mutant (C54Y) lacking DNA binding had minimal effect (Figure 4G). Moreover, SHLD1 or THAP1 overexpression in *Thap1*$^{-/-}$*Brca1*$^{\Delta 11}$ MEFs increased chromosomal aberrations to levels comparable to or higher than in *Brca1*$^{\Delta 11}$ parental cells (Figures 4H and S5D). In contrast to SHLD1, ectopic SHLD3 expression did not promote PARPi hypersensitivity in *Thap1*$^{-/-}$*Brca1*$^{\Delta 11}$ cells, despite normal focal accumulation (Figures S4C and S5E). Thus, THAP1-dependent *Shld1* transcription is essential for maintaining the functionality of Shieldin, but is not required for localizing the complex to DNA damage sites.

THAP1 promotes Immunglobulin Class-Switch Recombination

Uncontrolled activation of the 53BP1-RIF1-Shieldin pathway may compromise genome integrity during S/G2, but its normal function is uniquely required for NHEJ during CSR, a genome rearrangement process that initiates in G1 (Findlay et al., 2018; Ghezraoui et al., 2018; Gupta et al., 2018; Manis et al., 2004; Noordermeer et al., 2018; Petersen et al., 2001; Ward et al., 2004). Notably, we found that loss of THAP1 severely compromised CSR in cytokine-stimulated CH12-F3 mouse B cells, similar to inactivation of 53BP1, SHLD1 or SHLD3 (Figure 5A). These results revealed a hitherto unknown physiological function THAP1 outside of the developing nervous system in which it maintains *Shld1* expression to promote NHEJ.

Although Shieldin genes are epistatic with 53BP1 and RIF1 with respect to CSR, they are phylogenetically younger than the upstream components of the DNA end-protection pathway (Gupta et al., 2018). Indeed, it has been speculated that the evolution of Shieldin may have contributed to the emergence of a primitive form of CSR, with SHLD1 being the most recently evolved regulator (Gupta et al., 2018). Interestingly, based on homology data across diverse eukaryotes, we found that THAP1 evolved recently with components of the Shieldin complex (Figure 5B). It is therefore tempting to speculate that THAP1 might have co-evolved with Shieldin to regulate developmentally programmed NHEJ during CSR.

DISCUSSION

The Shieldin complex is a key enforcer of 53BP1-mediated DSB end protection, which promotes NHEJ but blocks HR and confers chemotherapy hypersensitivity in BRCA1-deficient cells (Mirman and de Lange, 2020; Setiaputra and Durocher, 2019). Intriguingly,

compared to other factors operating in the same pathway, such as 53BP1, RIF1 and REV7, the Shieldin complex components SHLD1, SHLD2 and SHLD3 are expressed at extremely low abundance (Gupta et al., 2018; Ochs et al., 2019). Here we demonstrated that the evolutionarily conserved transcription factor THAP1 acts in concert with co-regulators HCF1 and YY1 to promote basal transcription of the *SHLD1* gene in mammalian cells. Moreover, we showed that an over-abundance of THAP1 or SHLD1 destabilizes the genome, while a complete ablation abolishes productive CSR but rescues PARPi hypersensitivity in BRCA1 deficient cells. Our observation that loss of THAP1 restores HR and chemoresistance in both $Brca1^{\Delta 11}$ (resection-deficient) and $Brca1^{\Delta 11}Trp53bp1^{S25A}$ (resection-proficient, RAD51 loading-deficient) MEFs is consistent with Shieldin exerting anti-HR activities both pre- and post-resection. Similar to 53BP1 deficiency, loss of SHLD1 also rescues the embryonic lethality in BRCA1-deficient mice. Collectively, these observations suggest that low basal levels of SHLD1 suffice for NHEJ-mediated repair while hyper-activation disproportionately inhibits HR, highlighting the need for cells to fine-tune Shieldin activity in order to maintain genome stability.

Organisms with no clear orthologs for 53BP1, RIF1 or Shieldin also generally lack a recognizable orthologous *Brca1* gene (Figure 5B). Given that excessive end protection can potentially compromise genome stability, we propose that orthologs of BRCA1 might have evolved specifically to counteract 53BP1-RIF1-Shieldin activity, thereby balancing the requirement for inherently error-prone NHEJ against the overarching need for maximizing genome stability through high-fidelity DSB repair.

Surprisingly, unlike BRCA1-deficient MEFs and human cells, in which loss of THAP1 largely rescued PARPi-induced genomic instability, we observed the opposite effect in BRCA2-mutant mESCs. Accordingly, clinical data suggested that low expression of THAP1 correlated with better outcome in *BRCA2*-mutated patients with serious ovarian cancer. Consistently, we found that low SHLD1 expression also correlates with improved survival in BRCA2 deficient ovarian cancer (Figure S1J). We note that a similar observation has previously been made in mouse cells lacking PALB2, in which the existing vulnerability to PARPi was further exacerbated upon loss of 53BP1 (Bowman-Colin et al., 2013). More recently, it has been reported that restricting 53BP1 engagement at DSBs in the absence of BRCA2 significantly exacerbates PARPi hypersensitivity (Clements et al., 2020). Therefore, HR restoration in cells with an inhibited 53BP1-RIF1-Shieldin pathway seems to be contingent on RAD51 nucleofilament assembly, and productive assembly of the recombinase has been shown to limit the extent of end resection (Huang et al., 2018; Paiano et al., 2020). Therefore, it is possible that deletion of THAP1/SHLD1 or 53BP1 leads to excessive single-strand DNA in BRCA2-deficient cells, which in turn could increase genomic instability by engaging highly mutagenic RAD51-independent single strand annealing pathways (Ochs et al., 2016). In summary, our study suggests that THAP1 expression is a modifier and a potential predictive biomarker for DNA damaging chemotherapy responses in the context of BRCA1/2-deficient patients.

Limitations of the Study

Defects in DNA repair have been documented in various neurodevelopmental and neurogenerative diseases. Dystonia is a neurological condition characterized by involuntary muscle contractions that may manifest in a number of human syndromes. Of these, torsion dystonia 6 (DYT6) is caused by mutations in the transcription factor THAP1, suggesting abnormalities in gene regulation (Bressman et al., 2009; Djarmati et al., 2009; Fuchs et al., 2009). This study has uncovered a key role for THAP1 in the transcriptional control of SHLD1 expression. While our study clearly demonstrates that the THAP1-SHLD1 transcriptional network promotes DSB repair, it is important to note that such evidence does not demonstrate that unresolved DNA damage contributes to the abnormal neuronal activity responsible for DYT6 dystonia. In part, the difficulty in establishing cause and effect is due to the relative lack of mouse models that accurately recapitulate the involuntary muscle contractions found in human DYT6, and unknown genetic modifiers that protect against clinical expression of DYT6. Future studies will also be needed to determine whether symptomatic THAP1-linked dystonia (DYT6) is associated with measurable defects in DSB repair, which would have important implications for patient counseling and treatment.

STAR METHODS

RESOURCE AVAILABILITY

Lead Contact—Further information and requests for resources and reagents should be directed to and will be fulfilled by the Lead Contact, Andre Nussenzweig (andre_nussenzweig@nih.gov).

Materials Availability—All unique/stable reagents generated in this study are available from the Lead Contact with a completed Materials Transfer Agreement.

Data and code availability—The accession number for the datasets reported in this paper is available at GEO with accession number: GSE154729. All the original data for Figures 3, 4, S1, and S3–S5 are available on Mendeley (Mendeley Data: http://dx.doi.org/10.17632/35jfgtzkk4.1).

EXPERIMENTAL MODEL AND SUBJECT DETAILS

Mice—*Shld1*$^{-/-}$ mice were generated as described in Method Detail. *Brca1*$^{+/\Delta 11}$ (germline), *Brca1*$^{F\Delta 11/F\Delta 11}$; *CD19Cre* (conditional) mice were obtained from the NCI mouse repository. *Trp53bp1*$^{-/-}$ mice have been described (Ward et al., 2003). *Shld1*$^{-/-}$ *Brca1*$^{\Delta 11/\Delta 11}$ and *Trp53bp1*$^{-/-}$ *Brca1*$^{\Delta 11/\Delta 11}$ mice were generated by crossing *Shld1*$^{+/-}$ mice with *Brca1*$^{+/\Delta 11}$ mice or *Trp53bp1*$^{+/-}$ mice with *Brca1*$^{\Delta 11/+}$ mice, respectively. Male and female mice were used at 6–10 weeks of age. Mice were maintained in a specific pathogen–free (SPF) facility, and all breeding and experimentation followed protocol (20–042) approved by the National Institutes of Health Institutional Animal Care and Use Committee.

Mouse B cells—Resting primary B cells were isolated from the spleen using anti-CD43 microbeads (Miltenyi Biotec). Purified cells were resuspended in complete B cell medium containing 25 μg/mL LPS, 5 ng/mL IL-4 (both Sigma-Aldrich) and 0.5 μg/mL anti-CD180

(BD Biosciences) to stimulate proliferation and immunoglobulin class switch recombination (CSR). Successful *ex vivo* CSR was assayed on day 5 by flow cytometry following live cell staining using biotinylated anti-IgG1 and PE conjugated anti-B220 antibodies (BD Biosciences). Analysis of FACS data was done using FlowJo (version 10).

Cell lines—Cell lines used in this study are listed in the key resources table. Mouse embryonic fibroblasts (MEFs) were generated as previously described (Callen et al., 2020). The *Brca1*$^{\Delta 11}$ and *Brca1*$^{\Delta 11}$*Trp53bp1*^{S25A} MEFs were generated from E13.5 embryos and grown in Dulbecco's Modified Eagle's Medium (DMEM, GIBCO) supplemented with 15% heat-inactivated fetal bovine serum (FBS, Gemini Bio-Products) and 1% penicillin and streptomycin (GIBCO). To establish immortalized MEF cell lines, primary MEFs between passages 2–4 were transiently transfected with a vector encoding SV40 T-antigen (pCMV-SV40T). SV40-immortalized MEFs were routinely cultured in DMEM supplemented with 10 or 15% FBS. RPE1-hTERT *TP53*$^{-/-}$*BRCA1*$^{-/-}$ and RPE1-hTERT *TP53*$^{-/-}$ cells were kind gifts from Dr. Daniel Durocher (Lunenfeld-Tanenbaum Research Institute) and grown in Dulbecco's Modified Eagle's Medium (DMEM, GIBCO) supplemented with 10% heat-inactivated fetal bovine serum (FBS, Gemini Bio-Products), 1% L-glutamine (GIBCO), 1% penicillin and streptomycin (GIBCO). *Brca2*^{Y3308X} mES cells (Kuznetsov et al., 2008) were grown on 0.1% gelatin (Sigma) coated dishes in Dulbecco's Modified Eagle's Medium (DMEM, GIBCO) supplemented with 15% heat-inactivated fetal bovine serum (ESC-tested, Thermo Fisher Scientific), LIF (1000 U/ml) (Millipore), 0.1 mM MEM non-essential aminoacids, 1% glutamax and 55 μM β-mercaptoethanol. CH12-F3 cells were cultured in RPMI supplemented with 10% of heat-inactivated fetal bovine serum (FBS, Gemini Bio-Products), 10 mM HEPES (GIBCO), 1% penicillin and streptomycin (GIBCO), 1% L-glutamine (GIBCO), Sodium Pyruvate (1 mM) 55 μM β-mercaptoethanol and 5% NCTC-109 (ThermoFisher).

METHODS DETAILS

Generation of SHLD1 deficient mice

sgRNA target identification: The RefSeq sequence for *Shld1* (NM_028637.1) was downloaded from the UCSC Genome Browser and sgRNAs were designed against the protein coding exons using sgRNA Scorer 2.0 (Chari et al., 2017). Six candidate sgRNAs were tested in P19 mouse cells and editing rates were quantified using Illumina sequencing (Table S3), as previously described (Gooden et al., 2021). Candidates 1462 and 1465 were selected for transgenic mouse generation.

Pronuclear injections into C57/BL6NCr mouse zygotes: Synthetically modified versions of candidates 1462 and 1465 were obtained from Synthego and subsequently complexed with Cas9 protein. Cas9 protein was produced from the SP-Cas9 expression plasmid (Addgene #62731, http://n2t.net/addgene:62731; RRID:Addgene_62731) (D'Astolfo et al., 2015) by the protein expression laboratory at the Frederick National Lab for Cancer Research. SP-Cas9 was a gift from Niels Geijsen. Cas9 (50 ng/μl) and sgRNAs 1462 (100 ng/μl) and 1465 (100 ng/μl) were resuspended and complexed in 30 μl of Injection grade TE buffer and injected into ~700 embryos. Subsequently, 350 embryos were surgically

transferred to recipients within 24 h. In total, tails were clipped from 59 mice for genotyping.

Genration of Cell lines—Generation of Cas9-expressing *Brca1*$^{\Delta 11}$ and *Brca1*$^{\Delta 11}$*Trp53bp1*^{S25A} MEFs, cells were transduced with the LentiCas9-Blast vector (Addgene #52962) and transductants were selected with blasticidin. Cells were then seeded at low densities (200–400 cells, depending on the cell line) on 15-cm dishes and single colonies were isolated using glass cylinders. Cas9 expression was confirmed by immunoblotting.

Generation of CRISPR knockout MEF and human cell lines were carried out as follows: Individual sgRNA (see Table S3 for sgRNA sequence) were cloned into LentiCRISPRv2 (Addgene #52961). To produce and package infectious lentivirus, HEK293T cells (American Type Culture Collection) at 80% confluency were co-transfected with LentiCRISPRv2-sgRNA, pRSV-Rev, pMDLg-pRRE and pHCMVG. After 72 h, viral supernatant was collected and passed through a 0.45 μm filter. Wild-type MEFs, *Brca1*$^{\Delta 11}$ MEFs or *TP53*$^{-/-}$*BRCA1*$^{-/-}$ hTERT-RPE1 cells (1×10^5) were seeded in 6-well plates and transduced using the filtered viral supernatant along with polybrene (10 μg/ml). The packaging vectors were kind gifts from Dr. Shyam K. Sharan (NCI-Frederick, NIH). After 48 h, cells were subjected to puromycin selection (MEFs, 1.5 μg/ml; RPE1, 15 μg/ml) for five days. Thereafter, single cells were sorted into 96-well plates on a BD FACSAria UV instrument (BD Biosciences) and grown until colonies formed. Knockout clones were confirmed by Sanger sequencing of PCR amplicons of the targeted region that underwent editing. When different alleles of mutant clones had to be analysed, target regions were amplified by PCR using 50 ng genomic DNA in MyTaq Red mix (Bioline) according to manufacture instructions (primers are shown in Table S3). The amplicons were cloned using Zero Blunt TOPO PCR Cloning Kit (Thermo Fisher Scientific), and transformed into TOP10 or STBL3 chemically competent E. coli. (Thermo Fisher Scientific). Bacterial colonies containing plasmids with inserts were selected by colony-direct PCR, and were subsequently used for direct Sanger sequencing. The THABS deleted clone was generated by CRISPR/Cas9-mediated gene deletion. Two sgRNAs targeting sequences that flank the THABS sequences within *Shld1* promoter region were cloned into LentiCRISPRv2 (Addgene #52961, puromycin resistance) and LentiCRISPRv2 neo (Addgene #98292, neomycin resistance), respectively. One hundred thousand *Brca1*$^{\Delta 11}$ MEFs (14223) were co-infected with filtered viral supernatant of two sgRNAs. After 48 h, cells were subjected to puromycin (1.5 μg/ml) and G418 (1 mg/ml) selection for five days. Cells were then seeded at low densities (200–400 cells) on 15-cm dishes and single colonies were isolated using glass cylinders. The gRNA sequences and PCR primers for screening the deletions are provided in Table S3. PCR products spanning deletion sites were purified and confirmed with Sanger sequencing.

Generation of *Thap1*$^{-/-}$*Brca2*^{Y3308X} clones was performed as follows. Guide RNA against *Thap1* (see Table S3 for sgRNA sequence) was cloned into LentiCRISPRv2 with a Neo selection marker (Addgene #98292). *Brca2*^{Y3308X} mES cells (1×10^5) cells were seeded in 6-well plates and transduced using virus produced from HEK293T cells along with

polybrene (10 μg/ml). Thereafter, cells were selected with G418 (0.2 mg/ml). *Thap1*$^{-/-}$ clones were confirmed by Sanger sequencing as described above.

Trp53bp1$^{-/-}$, *Shld1*$^{-/-}$, and *Shld3*$^{-/-}$ CH12-F3 cells were generated as previously described (Gupta et al., 2018). *Thap1* mutant clones were edited through transient transfection with the pX330 (Addgene #42230) plasmid constructs expressing Cas9 and sgRNAs against *Thap1* (sgRNA: *Thap1*-sgRNA2, see Table S3), along with a plasmid encoding hCD4 (pcDNA3.1-Hygro-delta-hCD4), using an Amaxa Nucleofector II instrument (Lonza). Magnetic beads (STEMCELL Technologies 18052) were used to isolate hCD4^{+} cells 48 hour post-transfection. Thereafter, cells were grown for ~7 days and subcloned by single cell sorting on a BD FACSAria UV instrument (BD Biosciences). *Thap1*$^{-/-}$ clones were confirmed by Sanger sequencing as described above.

To generate GFP-SHLD3 expressing clones, *Thap1*$^{-/-}$*Brca1*$^{\Delta 11}$ MEFs were transduced with pCW-eGFP-SHLD3 (Addgene #114126) along with polybrene (10 μg/ml). Forty-eight hours after infection, the cells were treated with 1 μg/ml doxycycline for 24 h and single GFP^{+} cells were sorted into 96-well plates on a BD FACSAria UV instrument (BD Biosciences) and grown until colonies formed.

WT and *Thap1*$^{-/-}$*Brca1*$^{\Delta 11}$ MEFs expressing inducible exogenous THAP1 or SHLD1 were generated as follows. The PB-TRE-dCas9-VPR plasmid (Addgene #63800) was modified in which dCas9 was replaced by SnaBI, PacI and NotI restriction enzyme recognition sites. Thereafter, C-terminal Myc-Flag-tagged sgRNA target site-mutated version of the mouse *Thap1* cDNA (NM_199042) was inserted using SnaBI and PacI (PB-TRE-mTHAP1). Alternatively, C-terminal Flag-tagged mouse SHLD1 cDNA (NM_001358260.1) was inserted using SnaBI and NotI (PB-TRE-mSHLD1). Thap1 C54Y mutation (THAP1^{C54Y}) and sgRNA target site mutation in mouse *Thap1* cDNA was generated by Q5 Site-Directed Mutagenesis Kit (NEB, see Table S3 for primers). *WT* or *Thap1*$^{-/-}$*Brca1*$^{\Delta 11}$ MEFs (1×10^{6}) were seeded in 10 cm dish and cultured for 24 hours. Cells were subsequently transfected with 7 μg of PB-TRE-mTHAP1, PB-TRE-mTHAP1^{C54Y} or PB-TRE-mSHLD1 along with 1.4 μg of a transposase expressing plasmid. Fourty-eight hours after transfection, cells were subjected to selection with 250 μg/ml hygromycin (Thermo Fisher Scientific) for 5 days. Cells were then seeded at low densities (200–400 cells) on 15-cm dishes and single colonies were isolated using glass cylinders. Selected clones were cultured in medium containing 1 μg/ml doxycycline for the indicated amount of time, and THAP1/SHLD1 expression was confirmed by immunoblotting.

CRISPR–Cas9 screen—CRISPR–Cas9 screen was performed using genome-scale mouse Brie CRISPR knockout pooled library (Addgene #73633) (Doench et al., 2016). *Cas9*$^{+}$*Brca1*$^{\Delta 11}$ and *Cas9*$^{+}$*Brca1*$^{\Delta 11}$*Trp53bp1*^{S25A} MEFs were transduced at a multiplicity of infection (MOI) of 0.3 and 400-fold coverage of the library. Cells were then selected with puromycin for 3 days before treatment with the clinically-approved inhibitor Olaparib (PARPi, 100 nM) for a further 14 days. This dose corresponds with to the IC95 for the BRCA1-deficient cells. Surviving clones from each condition were collected, and genomic DNA (gDNA) was isolated (Blood & Cell Culture DNA Midi Kit, Qiagen) and subjected to PCR with Illumina-compatible primers, followed by Illumina sequencing. Genes enriched

or depleted in the PARPi-treated samples were determined with the MAGeCK software package version 0.5.9.2.

Multicolor growth competition assay (MCA)—One hundred thousand cells of two independent clones of Cas9-expressing *Brca1*$^{\Delta 11}$ MEFs (14223 and S12) were infected with either virus particles of NLS-mCherry LacZ-sgRNA or NLS-GFP GOI-sgRNA (*Thap1*, *Trp53bp1* or the empty vector), respectively. Ninety-six hours after transduction, mCherry- and GFP-expressing cells were mixed 1:1 and 5×10^5 cells were seeded with or without PARPi (Olaparib, 100 nM) in 100 mm dishes. During the course of the experiment, cells were subcultured when they approach confluency was reached. PARPi-containing medium was replaced every three days. Cells were analyzed on the day of initial plating (t = 0) and on days 3, 6, 9 and 14 using the flow cytometer (LSRFortessa; BD) and the percentage of GFP- and mCherry-positive cells were analyzed using FlowJo software (Tree Star). LIVE/DEAD discrimination was performed by staining with 1 μg/ml of 4'6-diamidino-2-phenylindole (DAPI, Invitrogen).

Immunoblotting and Immunofluorescence—Western blotting was performed as described previously (Zong et al., 2019). Briefly, cells were collected and lysed in a buffer containing 50 mM Tris-HCl (pH 7.5), 200 mM NaCl, 5% Tween-20, 0.5% NP-40, 2 mM PMSF, 2.5 mM b-glycerophosphate (all from Sigma) and protease inhibitor cocktail tablet (complete Mini, Roche Diagnostics). Equal amounts of protein were loaded into precast mini-gels (Invitrogen) and resolved by SDS-PAGE. Proteins were blotted onto a nitrocellulose membrane, blocked with 5% membrane blocking agent (GE Healthcare) in TBS and incubated with the corresponding primary antibody. Primary antibodies were used at the following dilutions: anti-pRPA32 (p Ser4, Ser8, 1:1000, Novus), anti-Flag (1:1000, Sigma) and anti-Tubulin (1:10,000, Sigma). Fluorescent secondary antibodies were used at a dilution of 1:15,000 (Li-Cor Biosciences). Detection of protein bands was performed by fluorescence imaging using a Li-Cor Odyssey CLx imaging system (Li-Cor Biosciences).

For immunofluorescence staining, MEFs were grown on 18 mm × 18 mm glass coverslips. Prior to γ-irradiation (^{137}Cs Mark 1 irradiator, JL Shepherd), cells were incubated with 10 μM EdU (Invitrogen) for 20 min. Following irradiation, cells were allowed to recover for 1 hour or 4 hours. Thereafter, cells were pre-extracted (20 mM HEPES, 50 mM NaCl, 3 mM $MgCl_2$, 0.3 M sucrose, 0.2% Triton X-100) on ice for 5 min to remove soluble nuclear proteins. Extracted samples were fixed (4% para-formaldehyde), permeabilized (0.5% Triton X-100), incubated with the indicated primary antibodies followed by appropriate fluorochrome-conjugated secondary antibodies (Invitrogen). Next, click-IT chemistry was performed as per manufacturer's instructions (Thermo Fisher Scientific) and DNA was counterstained with DAPI (Thermo Fisher Scientific). Images were captured at 63X magnification with an AxioCam MRc5 mounted on an Axio Observer Z1 epifluorescence microscope (Zeiss) or at 40x magnification on a Lionheart LX automated microscope (BioTek Instruments, Inc.). Quantification of nuclear foci and total nuclear intensity was performed using the Gen5 spot analysis software (BioTek). The antibodies used for standard immunofluorescence experiments were anti-RIF1 (1:5,000, gift of Davide Robbiani,

Rockefeller University), anti-53BP1 (1:1000, Novus), anti-RAD51 (1:250, Abcam), anti-RPA (1:2,000, Cell Signaling), and anti-GFP (1:500, Roche).

Analysis of metaphase spreads—Activated cycling B cells, asynchronous MEFs and mESCs were treated with 0.5 μM or 1 μM PARPi (Olaparib, Selleckchem) for 16 hours, subsequently arrested at mitosis with 0.1 mg/ml colcemid (Roche) for 1 h (B cells, mESCs) or 8 h (MEFs). Metaphase chromosome spreads were prepared as previously described (Zong et al., 2019). Briefly, cells were first incubated with a prewarmed hypotonic solution (0.75 M KCl, Sigma) for 20 min at 37 °C. Thereafter, suspensions of single cells were fixed with a solution mixture containing methanol and glacial acetic acid (3:1 ratio). Following initial fixation, cells were further washed extensively with the same fixative solution. Finally, samples were dropped onto slides in a humidified chamber (Thermotron Industries).

To visualize metaphase chromosomes by fluorescence in-situ hybridization (FISH), samples immobilized on slides were treated with pepsin (5–10 μg/ml in 0.01 N HCl, 5 min at 37 °C), washed, dehydrated with ethanol, briefly denatured (80 °C, 1 min 15 sec) in a slide moat (Boekel Scientific) and incubated with a commercially available Cy3-labeled $(CCCTAA)_3$ peptide nucleic acid probe (PNA Bio) recognizing mammalian telomere sequences. After extensive washes, DNA was counterstained with DAPI. Images were acquired using the Metafer automated scanning and imaging platform (MetaSystems). Fifty to a hundred metaphases were scored for the presence of chromosomal aberrations.

Cell viability assays—Clonogenic survival for a given treatment was calculated relative to the plating efficiency in non-treated controls. To determine cell growth and viability, MEFs were plated in 6-well plates (10,000 per well) and treated continuously with different doses of PARPi or cisplatin (Sigma) for 7 days. The drug-containing medium was replenished every three days and cells were subcultured when they approach confluency. Cell viability was determined using the CellTiter-Glo Luminescent Cell Viability Assay (Promega) as per manufacturer's instructions.

Nascent RNA-seq—Nascent RNA sequencing was performed as previously described (Canela et al., 2019). Four million MEFs were labeled with 0.5 mM 5-ethynyl uridine (EU) for 30 min. Total RNA was extracted using TRIzol (Ambion). The NEBNext rRNA Depletion kit (human/mouse/rat) (New England Biosciences) was used to deplete rRNA from 1 μg of total RNA prior to sample biotinylation through Click-it reactions (Click-iT Nascent RNA Capture Kit, ThermoFisher C10365) as per the manufacturer's specification. First-strand cDNA synthesis of the captured nascent RNA was done using the SuperScript VILO cDNA synthesis kit (Invitrogen), followed by AMPure XP purification (1.8X) and elution in (20 μl), Thereafter, second-strand cDNA synthesis was carried out in a total reaction volume of 30 μl that contained 0.6 mM dNTP, 1.2 mM of dUTP, 2 units of RNase H (Invitrogen) and 20 units of E. coli DNA polymerase I (Invitrogen), for 2.5 hr at 16°C. Double stranded cDNA was cleaned using 1.8X Agencourt AMPure XP beads and eluted in 20 μl of EB that was used for end-repair. End-repair was performed in 50 μl of T4 ligase reaction buffer containing 0.4 mM of dNTPs, 3 units of T4 DNA polymerase (NEB), 9 units of T4 Polynucleotide Kinase (NEB) and 1 unit of Klenow fragment (NEB) at 24°C for 30 min in a ThermoMixer C at 400 rpm. End-repair

reaction was cleaned using 1.8X Agencourt AMPure XP beads and eluted in 15 μl of EB that was used for A-tailing reaction in 30 μl of NEBNext dA-Tailing reaction buffer (NEB) with 7.5 units of Klenow fragment exo-(NEB) at 37°C for 30 min. The 30 μl of the A-tailing reaction were mixed with Quick Ligase buffer 2X (NEB), 3,000 units of Quick ligase and 5 nM of annealed adaptor (Illumina truncated adaptor) in a volume of 75 μl and incubated at 25°C for 20 min. The adaptor was prepared by annealing the following HPLC-grade oligos: 5′-Phos/GATCGGAAGAGCACACGTCT-3′and 5′-ACACTCTTTCCCTACACGACGCTCTTCCGATC*T-3′ (*phosphorothioate bond). The ligation reaction was terminated by adding 50mM of EDTA and cleaned with 1.8X Agencourt AMPure XP beads and eluted in 15 μl of EB. Thereafter, samples were treated with 0.5 units of Uracil-DNA glycosylase (Thermofisher) for 15 min at 37°C and used for PCR amplification in a 50 μl reaction volume containing 1 μM of TruSeq barcoded primer p5, AATGATACGGCGACCACCGAGATCTACACNNNNNNNNACACTCTTTCCCTACACGACGCTCTTCCGATC*T, TruSeq barcoded primer p7, CAAGCAGAAGACGGCATACGAGANNNNNNNNGTGACTGGAGTTCAGACGTGTGCTCTTCCGATC*T, (NNNNNNNN represents barcode and * a phosphothiorate bond), and 2X Kapa HiFi HotStart Ready mix (Kapa Biosci-ences). The temperature settings during the PCR amplification were 45 s at 98°C followed by 15 cycles of 15 s at 98°C, 30 s at 63°C, 30 s at 72°C and a final 5 min extension at 72°C. PCR reactions were cleaned with Agencourt AMPure XP beads (Beckman Coulter), run on a 2% agarose gel and a smear of 200–500bp was cut and gel purified using QIAquick Gel Extraction Kit (QIAGEN). Library concentration was determined with KAPA Library Quantification Kit for Illumina Platforms (Kapa Biosystems). Sequencing was performed on the Illumina Nextseq500 (75 bp single end reads).

ChIP-Seq—ChIP-seq was performed as described previously (Shinoda et al., 2019) with a rabbit polyclonal antibody against THAP1 (Proteintech, 12584–1-AP). Twenty million MEFs were fixed in fresh media by adding 37% formaldehyde (F1635, Sigma) to attain a final concentration of 1% and incubated at 37°C for 10 min. Fixation was quenched by addition of 1 M glycine (Sigma) in PBS at a final concentration of 125 mM. Cells were washed twice with cold PBS and pellets were snap frozen in dry ice and stored at −80°C. Fixed cell pellets were thawed on ice and resuspended in 2 ml of cold RIPA buffer (10 mM TrisHCl pH 7.5, 1 mM EDTA, 0.1% SDS, 0.1% sodium deoxycholate, 1% Triton X-100, supplemented with proteinase inhibitor (Complete Mini EDTA free, Roche)). Sonication was performed using the Covaris S220 sonicator at duty cycle 20%, peak incident power 175, cycle/burst 200 for 30 cycles of 60 s sonication and 30 s of pause at 4°C. Chromatin was clarified by centrifugation at 21,000 g at 4°C for 10 min and precleared with 80 μl prewashed Dynabeads protein A (ThermoFisher) for 30 min at 4°C. 40 μl of prewashed Dynabeads protein A were incubated with 10 μg of antibody in 100 μl of PBS for 30 min at room temperature under continuous mixing, washed twice in PBS for 5 min and added to 1 ml of chromatin followed by overnight incubation at 4°C on a rotator. Beads were then collected in a magnetic separator (DynaMag-2 Invitrogen), washed twice with cold RIPA buffer, twice with RIPA buffer containing 0.3 M NaCl, twice with LiCl buffer (0.25 M LiCl, 0.5% Igepal-630, 0.5% sodium deoxycholate), once with TE (10 mM Tris pH 8.0, 1mM EDTA) plus 0.2% Triton X-100, and once with TE. Crosslinking was reversed

by incubating the beads at 65°C for 4 hr in the presence of 0.3% SDS and 1 mg/ml of Proteinase K (Ambion). DNA was purified using Zymo ChIP DNA clean and concentrator kit (Zymo Research) and eluted in 20 μl. The entire ChIP DNA was used to prepare Illumina sequencing libraries. End-repair was performed in 75 μl of T4 ligase reaction buffer, 0.4 mM of dNTPs, 4 U of T4 DNA polymerase (NEB), 13.5 U of T4 Polynucleotide Kinase (NEB) and 1.5 U of Klenow fragment (NEB) at 24°C for 30 min in a ThermoMixer C at 400 rpm. End-repair reaction was cleaned using 2X Agencourt AMPure XP beads and eluted in 16.5 μl of EB that was used for A-tailing reaction in 20 μl of NEBNext dA-Tailing reaction buffer (NEB) with 7.5 U of Klenow fragment exo-(NEB) at 37°C for 30 min. The 20 μl of the A-tailing reaction was mixed with Quick Ligase buffer 2X (NEB), 3,000 U of Quick ligase and 5 nM of annealed adaptor (Illumina truncated adaptor) in a volume of 50 μl and incubated at 25°C for 20 min. Ligation was stopped by adding 50 mM of EDTA and cleaned with 1.8X Agencourt AM- Pure XP beads and eluted in 15 μl of EB that was used for PCR amplification in a 50 μl reaction with 1 μM primers TruSeq barcoded primer p5, TruSeq barcoded primer p7, and 2X Kapa HiFi HotStart Ready mix (Kapa Biosciences). The temperature settings during the PCR amplification were 45 s at 98°C followed by 14 cycles of 15 s at 98°C, 30 s at 63°C, 30 s at 72°C and a final 5 min extension at 72°C. PCR reactions were cleaned with Agencourt AMPure XP beads (Beckman Coulter), run on a 2% agarose gel and a smear of 200–500bp was cut and gel purified using QIAquick Gel Extraction Kit (QIAGEN). Library concentration was determined with KAPA Library Quantification Kit for Illumina Platforms (Kapa Biosystems). Sequencing was performed on the Illumina Nextseq500 (75bp single-end reads).

Class switch recombination (CSR) assay in CH12-F3 cells—The mouse B lymphocyte cell line CH12-F3 cells was cultured and stimulated with 250 ng/ml CD40L, 10 ng/ml IL4 and 1 ng/ml TGFβ (CIT) to induce immunoglobulin class switching from IgM to IgA. For FACS analysis of CSR efficiency, live CH12-F3 cells were labeled with FITC-conjugated anti-IgM (ThermoFisher Scientific) and PE-conjugated anti-IgA (Southern Biotech) antibodies. All analyses were performed on FACS CantoII (BD Biosciences).

RNA extraction and quantitative real-time PCR (RT-PCR)—Total RNA was extracted from MEFs using TRIzol reagent (Thermo Fisher, 15596018). Total RNA was reverse transcribed with iSCRIPT Advanced cDNA Synthesis Kit (Bio-Rad, 1725037) following manufacturer's instructions. The resulting cDNA was diluted to 10 times and used for quantitative real-time PCR (qRT-PCR) analyses with specific primer sets (Bio-Rad, Actb qMmuCED0027505; Shld1 (1110034G24Rik) qMmuCID0014233) in a final volume of 20 μl reaction which contained 10 μl of SsoAdvanced™ Universal SYBR Green Supermix (Biorad, 1725271), 3 μl of cDNA and final volume made up with water. qRT-PCR was performed in triplicate wells per sample on a CFX96 Real-Time System (Biorad).

Traffic Light reporter assay—Cells were infected with the pCVL.TrafficLightReporter.Ef1a.Puro lentivirus (Addgene #31482) at a low MOI (0.3–0.5) and selected with puromycin (1.5 μg/μl). Cells (7×10^5) were nucleofected with 5 μg of pCVL.SFFV.d14GFP.Ef1a.HA.NLS.Sce(opt).T2A.TagBFP plasmid DNA (Addgene #32627) with Mouse Embryonic Fibroblast Nucleofector Kit 2 (Lonza) using program

A-023 on a Nucleofector IIb (Lonza). After 72 h, GFP fluorescence was assessed in BFP-positive cells using the flow cytometer (LSRFortessa; BD).

TCGA analysis—Publicly available TCGA ovarian serous cystadenocarcinoma data on cBioportal (Cerami et al., 2012; Gao et al., 2013) were queried for *THAP1* and *SHLD1* expression data. Other clinical characteristics and information on *BRCA1* and *BRCA2* gene or expression alteration were also extracted for the 316 ovarian carcinoma tumors in the cohort (Cancer Genome Atlas Research, 2011). In total, 38 carcinomas with a *BRCA1* mutation and 34 carcinomas harboring a *BRCA2* mutation were isolated from the cohort and used for further analysis. All calculations were performed using and Graph Pad Prism v.7.0.

Analysis of orthologous genes between species—Orthology presnce/absence data is based on Ensembl orthology data versions 98, 99 and 100 including human Ensembl genes used to mine Ensembl orthologs. Drosophila and Nematostella genes that were found to be orthologs of the human genes were used to further mine Ensembl Metazoa for additional animal orthologs, and human genes were further used to mine Pan-compara orthologs which includes taxa not present in the standard Ensembl dataset. A minimum of 15% identity of both query gene and target gene were required to avoid false positives.

Previously published RNA-seq and ChIP-seq datasets used in this study—RNA-seq and ChIP-seq datasets for *Thap1*$^{-/-}$ mESC were obtained from GSE86911(Aguilo et al., 2017). RNA-seq and ChIP-seq datasets for *Yy1*$^{flox/flox}$ TAT-Cre primary B cells were obtained from GSE145161(Nandi et al., 2020b). ChIP-seq dataset for YY1 in mESC were from GSE68195 (Sigova et al., 2015). RNA-seq dataset for hepatocytes of *Hcfc1*$^{HepKO/Y}$ mice were obtained from GSE115768 (Minocha et al., 2019). ChIP-seq dataset for HCF1 in mESC were from the Mouse ENCODE Project (GSE36030) (Mouse et al., 2012; Yue et al., 2014). ChIP-seq dataset for THAP1 in K562 cells were obtained from GSE32465 (Gertz et al., 2013). ChIP-seq data for HCF1 and YY1 in K562 cells were obtained from GSE31477(Consortium, 2012).

QUANTIFICATION AND STATISTICAL ANALYSIS

Statistical analyses—Unless indicated, all data are presented as individual replicates. The total number of replicates, mean and error bars are explained in the figure legends. The statistical tests (Student's, Welch's, one-way ANOVA and log-rank) and resultant P values (represented by asterisks) are indicated in the figure legends and/or figure panels and were calculated using GraphPad Prism and R software (ns = $p > 0.05$; * = $p < 0.05$; ** = $p < 0.01$; *** = $p < 0.001$).

Supplementary Material

Refer to Web version on PubMed Central for supplementary material.

Acknowledgements

We thank Sergio Ruiz Macias, Eros Lazzerini Denchi, and Nussenzweig lab members for stimulating discussions; Daniel Durocher for the *TP53*$^{-/-}$*BRCA1*$^{-/-}$ human RPE1 cell line; Panagiotis A. Konstantinopoulos for assistance with TCGA analysis; K.S. was supported by a fellowship from the Uehara Memorial Foundation; Sequencing were

supported from the NCI CCR Genomics Core; Flow cytometry analyses and sorting were performed at the NCI CCR LGI Flow Cytometry Core; *Shld1*$^{-/-}$ mice were generated at the NCI Genome Modification Core, Laboratory Animal Sciences Program; The A.N. laboratory is supported by the Intramural Research Program of the NIH, an Ellison Medical Foundation Senior Scholar in Aging Award (AG-SS- 2633-11), the Department of Defense Idea Expansion (W81XWH-15-2-006) and Breakthrough (W81XWH-16-1-599) Awards, the Alex Lemonade Stand Foundation Award, and an NIH Intramural FLEX Award.

REFERENCES

Aguilo F, Zakirova Z, Nolan K, Wagner R, Sharma R, Hogan M, Wei C, Sun Y, Walsh MJ, Kelley K, et al. (2017). THAP1: Role in Mouse Embryonic Stem Cell Survival and Differentiation. Stem Cell Reports 9, 92–107. [PubMed: 28579396]

Barazas M, Annunziato S, Pettitt SJ, de Krijger I, Ghezraoui H, Roobol SJ, Lutz C, Frankum J, Song FF, Brough R, et al. (2018). The CST Complex Mediates End Protection at Double-Strand Breaks and Promotes PARP Inhibitor Sensitivity in BRCA1-Deficient Cells. Cell Rep 23, 2107–2118. [PubMed: 29768208]

Belotserkovskaya R, Raga Gil E, Lawrence N, Butler R, Clifford G, Wilson MD, and Jackson SP (2020). PALB2 chromatin recruitment restores homologous recombination in BRCA1-deficient cells depleted of 53BP1. Nat Commun 11, 819. [PubMed: 32041954]

Blanchard A, Ea V, Roubertie A, Martin M, Coquart C, Claustres M, Beroud C, and Collod-Beroud G (2011). DYT6 dystonia: review of the literature and creation of the UMD Locus-Specific Database (LSDB) for mutations in the THAP1 gene. Hum Mutat 32, 1213–1224. [PubMed: 21793105]

Boersma V, Moatti N, Segura-Bayona S, Peuscher MH, van der Torre J, Wevers BA, Orthwein A, Durocher D, and Jacobs JJL (2015). MAD2L2 controls DNA repair at telomeres and DNA breaks by inhibiting 5' end resection. Nature 521, 537–540. [PubMed: 25799990]

Bouwman P, Aly A, Escandell JM, Pieterse M, Bartkova J, van der Gulden H, Hiddingh S, Thanasoula M, Kulkarni A, Yang Q, et al. (2010). 53BP1 loss rescues BRCA1 deficiency and is associated with triple-negative and BRCA-mutated breast cancers. Nat Struct Mol Biol 17, 688–695. [PubMed: 20453858]

Bowman-Colin C, Xia B, Bunting S, Klijn C, Drost R, Bouwman P, Fineman L, Chen X, Culhane AC, Cai H, et al. (2013). Palb2 synergizes with Trp53 to suppress mammary tumor formation in a model of inherited breast cancer. Proc Natl Acad Sci U S A 110, 8632–8637. [PubMed: 23657012]

Bressman SB, Raymond D, Fuchs T, Heiman GA, Ozelius LJ, and Saunders-Pullman R (2009). Mutations in THAP1 (DYT6) in early-onset dystonia: a genetic screening study. Lancet Neurol 8, 441–446. [PubMed: 19345147]

Bunting SF, Callen E, Wong N, Chen HT, Polato F, Gunn A, Bothmer A, Feldhahn N, Fernandez-Capetillo O, Cao L, et al. (2010). 53BP1 inhibits homologous recombination in Brca1-deficient cells by blocking resection of DNA breaks. Cell 141, 243–254. [PubMed: 20362325]

Byrum AK, Vindigni A, and Mosammaparast N (2019). Defining and Modulating 'BRCAness'. Trends Cell Biol 29, 740–751. [PubMed: 31362850]

Callen E, Di Virgilio M, Kruhlak MJ, Nieto-Soler M, Wong N, Chen HT, Faryabi RB, Polato F, Santos M, Starnes LM, et al. (2013). 53BP1 mediates productive and mutagenic DNA repair through distinct phosphoprotein interactions. Cell 153, 1266–1280. [PubMed: 23727112]

Callen E, Zong D, Wu W, Wong N, Stanlie A, Ishikawa M, Pavani R, Dumitrache LC, Byrum AK, Mendez-Dorantes C, et al. (2020). 53BP1 Enforces Distinct Pre- and Post-resection Blocks on Homologous Recombination. Mol Cell 77, 26–38 e27. [PubMed: 31653568]

Cancer Genome Atlas Research, N. (2011). Integrated genomic analyses of ovarian carcinoma. Nature 474, 609–615. [PubMed: 21720365]

Canela A, Maman Y, Huang SN, Wutz G, Tang W, Zagnoli-Vieira G, Callen E, Wong N, Day A, Peters JM, et al. (2019). Topoisomerase II-Induced Chromosome Breakage and Translocation Is Determined by Chromosome Architecture and Transcriptional Activity. Mol Cell 75, 252–266 e258. [PubMed: 31202577]

Cerami E, Gao J, Dogrusoz U, Gross BE, Sumer SO, Aksoy BA, Jacobsen A, Byrne CJ, Heuer ML, Larsson E, et al. (2012). The cBio cancer genomics portal: an open platform for exploring multidimensional cancer genomics data. Cancer Discov 2, 401–404. [PubMed: 22588877]

Certo MT, Ryu BY, Annis JE, Garibov M, Jarjour J, Rawlings DJ, and Scharenberg AM (2011). Tracking genome engineering outcome at individual DNA breakpoints. Nat Methods 8, 671–676. [PubMed: 21743461]

Chari R, Yeo NC, Chavez A, and Church GM (2017). sgRNA Scorer 2.0: A Species-Independent Model To Predict CRISPR/Cas9 Activity. ACS Synth Biol 6, 902–904. [PubMed: 28146356]

Charlesworth G, Bhatia KP, and Wood NW (2013). The genetics of dystonia: new twists in an old tale. Brain 136, 2017–2037. [PubMed: 23775978]

Chavez A, Scheiman J, Vora S, Pruitt BW, Tuttle M, E PRI, Lin S, Kiani S, Guzman CD, Wiegand DJ, et al. (2015). Highly efficient Cas9-mediated transcriptional programming. Nat Methods 12, 326–328. [PubMed: 25730490]

Cheng F, Walter M, Wassouf Z, Hentrich T, Casadei N, Schulze-Hentrich J, Barbuti P, Krueger R, Riess O, Grundmann-Hauser K, et al. (2020). Unraveling Molecular Mechanisms of THAP1 Missense Mutations in DYT6 Dystonia. J Mol Neurosci 70, 999–1008. [PubMed: 32112337]

Clairmont CS, Sarangi P, Ponnienselvan K, Galli LD, Csete I, Moreau L, Adelmant G, Chowdhury D, Marto JA, and D'Andrea AD (2020). TRIP13 regulates DNA repair pathway choice through REV7 conformational change. Nat Cell Biol 22, 87–96. [PubMed: 31915374]

Clements KE, Schleicher EM, Thakar T, Hale A, Dhoonmoon A, Tolman NJ, Sharma A, Liang X, Imamura Kawasawa Y, Nicolae CM, et al. (2020). Identification of regulators of poly-ADP-ribose polymerase inhibitor response through complementary CRISPR knockout and activation screens. Nat Commun 11, 6118. [PubMed: 33257658]

Clouaire T, Roussigne M, Ecochard V, Mathe C, Amalric F, and Girard JP (2005). The THAP domain of THAP1 is a large C2CH module with zinc-dependent sequence-specific DNA-binding activity. Proc Natl Acad Sci U S A 102, 6907–6912. [PubMed: 15863623]

Cong L, Ran FA, Cox D, Lin S, Barretto R, Habib N, Hsu PD, Wu X, Jiang W, Marraffini LA, et al. (2013). Multiplex genome engineering using CRISPR/Cas systems. Science 339, 819–823. [PubMed: 23287718]

Consortium, E.P. (2012). An integrated encyclopedia of DNA elements in the human genome. Nature 489, 57–74. [PubMed: 22955616]

D'Astolfo DS, Pagliero RJ, Pras A, Karthaus WR, Clevers H, Prasad V, Lebbink RJ, Rehmann H, and Geijsen N (2015). Efficient intracellular delivery of native proteins. Cell 161, 674–690. [PubMed: 25910214]

Dai Y, Zhang F, Wang L, Shan S, Gong Z, and Zhou Z (2020). Structural basis for shieldin complex subunit 3-mediated recruitment of the checkpoint protein REV7 during DNA double-strand break repair. J Biol Chem 295, 250–262. [PubMed: 31796627]

Dev H, Chiang TW, Lescale C, de Krijger I, Martin AG, Pilger D, Coates J, Sczaniecka-Clift M, Wei W, Ostermaier M, et al. (2018). Shieldin complex promotes DNA end-joining and counters homologous recombination in BRCA1-null cells. Nat Cell Biol 20, 954–965. [PubMed: 30022119]

Djarmati A, Schneider SA, Lohmann K, Winkler S, Pawlack H, Hagenah J, Bruggemann N, Zittel S, Fuchs T, Rakovic A, et al. (2009). Mutations in THAP1 (DYT6) and generalised dystonia with prominent spasmodic dysphonia: a genetic screening study. Lancet Neurol 8, 447–452. [PubMed: 19345148]

Doench JG, Fusi N, Sullender M, Hegde M, Vaimberg EW, Donovan KF, Smith I, Tothova Z, Wilen C, Orchard R, et al. (2016). Optimized sgRNA design to maximize activity and minimize off-target effects of CRISPR-Cas9. Nat Biotechnol 34, 184–191. [PubMed: 26780180]

Dull T, Zufferey R, Kelly M, Mandel RJ, Nguyen M, Trono D, and Naldini L (1998). A third-generation lentivirus vector with a conditional packaging system. J Virol 72, 8463–8471. [PubMed: 9765382]

Findlay S, Heath J, Luo VM, Malina A, Morin T, Coulombe Y, Djerir B, Li Z, Samiei A, Simo-Cheyou E, et al. (2018). SHLD2/FAM35A co-operates with REV7 to coordinate DNA double-strand break repair pathway choice. EMBO J 37.

Frederick NM, Shah PV, Didonna A, Langley MR, Kanthasamy AG, and Opal P (2019). Loss of the dystonia gene Thap1 leads to transcriptional deficits that converge on common pathogenic pathways in dystonic syndromes. Hum Mol Genet 28, 1343–1356. [PubMed: 30590536]

Fuchs T, Gavarini S, Saunders-Pullman R, Raymond D, Ehrlich ME, Bressman SB, and Ozelius LJ (2009). Mutations in the THAP1 gene are responsible for DYT6 primary torsion dystonia. Nat Genet 41, 286–288. [PubMed: 19182804]

Gao J, Aksoy BA, Dogrusoz U, Dresdner G, Gross B, Sumer SO, Sun Y, Jacobsen A, Sinha R, Larsson E, et al. (2013). Integrative analysis of complex cancer genomics and clinical profiles using the cBioPortal. Sci Signal 6, pl1. [PubMed: 23550210]

Gao S, Feng S, Ning S, Liu J, Zhao H, Xu Y, Shang J, Li K, Li Q, Guo R, et al. (2018). An OB-fold complex controls the repair pathways for DNA double-strand breaks. Nat Commun 9, 3925. [PubMed: 30254264]

Gertz J, Savic D, Varley KE, Partridge EC, Safi A, Jain P, Cooper GM, Reddy TE, Crawford GE, and Myers RM (2013). Distinct properties of cell-type-specific and shared transcription factor binding sites. Mol Cell 52, 25–36. [PubMed: 24076218]

Ghezraoui H, Oliveira C, Becker JR, Bilham K, Moralli D, Anzilotti C, Fischer R, Deobagkar-Lele M, Sanchiz-Calvo M, Fueyo-Marcos E, et al. (2018). 53BP1 cooperation with the REV7-shieldin complex underpins DNA structure-specific NHEJ. Nature 560, 122–127. [PubMed: 30046110]

Gooden AA, Evans CN, Sheets TP, Clapp ME, and Chari R (2021). dbGuide: a database of functionally validated guide RNAs for genome editing in human and mouse cells. Nucleic Acids Res 49, D871–D876. [PubMed: 33051688]

Gupta R, Somyajit K, Narita T, Maskey E, Stanlie A, Kremer M, Typas D, Lammers M, Mailand N, Nussenzweig A, et al. (2018). DNA Repair Network Analysis Reveals Shieldin as a Key Regulator of NHEJ and PARP Inhibitor Sensitivity. Cell 173, 972–988 e923. [PubMed: 29656893]

He YJ, Meghani K, Caron MC, Yang C, Ronato DA, Bian J, Sharma A, Moore J, Niraj J, Detappe A, et al. (2018). DYNLL1 binds to MRE11 to limit DNA end resection in BRCA1-deficient cells. Nature 563, 522–526. [PubMed: 30464262]

Hollstein R, Reiz B, Kotter L, Richter A, Schaake S, Lohmann K, and Kaiser FJ (2017). Dystonia-causing mutations in the transcription factor THAP1 disrupt HCFC1 cofactor recruitment and alter gene expression. Hum Mol Genet 26, 2975–2983. [PubMed: 28486698]

Huang TH, Fowler F, Chen CC, Shen ZJ, Sleckman B, and Tyler JK (2018). The Histone Chaperones ASF1 and CAF-1 Promote MMS22L-TONSL-Mediated Rad51 Loading onto ssDNA during Homologous Recombination in Human Cells. Mol Cell 69, 879–892 e875. [PubMed: 29478807]

Jaspers JE, Kersbergen A, Boon U, Sol W, van Deemter L, Zander SA, Drost R, Wientjens E, Ji J, Aly A, et al. (2013). Loss of 53BP1 causes PARP inhibitor resistance in Brca1-mutated mouse mammary tumors. Cancer Discov 3, 68–81. [PubMed: 23103855]

Karanam K, Kafri R, Loewer A, and Lahav G (2012). Quantitative live cell imaging reveals a gradual shift between DNA repair mechanisms and a maximal use of HR in mid S phase. Mol Cell 47, 320–329. [PubMed: 22841003]

Karolchik D, Hinrichs AS, Furey TS, Roskin KM, Sugnet CW, Haussler D, and Kent WJ (2004). The UCSC Table Browser data retrieval tool. Nucleic Acids Res 32, D493–496. [PubMed: 14681465]

Kent WJ, Sugnet CW, Furey TS, Roskin KM, Pringle TH, Zahler AM, and Haussler D (2002). The human genome browser at UCSC. Genome Res 12, 996–1006. [PubMed: 12045153]

Kuhar R, Gwiazda KS, Humbert O, Mandt T, Pangallo J, Brault M, Khan I, Maizels N, Rawlings DJ, Scharenberg AM, et al. (2014). Novel fluorescent genome editing reporters for monitoring DNA repair pathway utilization at endonuclease-induced breaks. Nucleic Acids Res 42, e4. [PubMed: 24121685]

Kuznetsov SG, Liu P, and Sharan SK (2008). Mouse embryonic stem cell-based functional assay to evaluate mutations in BRCA2. Nat Med 14, 875–881. [PubMed: 18607349]

Langmead B, Trapnell C, Pop M, and Salzberg SL (2009). Ultrafast and memory-efficient alignment of short DNA sequences to the human genome. Genome Biol 10, R25. [PubMed: 19261174]

Li W, Xu H, Xiao T, Cong L, Love MI, Zhang F, Irizarry RA, Liu JS, Brown M, and Liu XS (2014). MAGeCK enables robust identification of essential genes from genome-scale CRISPR/Cas9 knockout screens. Genome Biol 15, 554. [PubMed: 25476604]

Ling AK, Munro M, Chaudhary N, Li C, Berru M, Wu B, Durocher D, and Martin A (2020). SHLD2 promotes class switch recombination by preventing inactivating deletions within the Igh locus. EMBO Rep 21, e49823. [PubMed: 32558186]

Malewicz M, and Perlmann T (2014). Function of transcription factors at DNA lesions in DNA repair. Exp Cell Res 329, 94–100. [PubMed: 25173987]

Manis JP, Morales JC, Xia Z, Kutok JL, Alt FW, and Carpenter PB (2004). 53BP1 links DNA damage-response pathways to immunoglobulin heavy chain class-switch recombination. Nat Immunol 5, 481–487. [PubMed: 15077110]

Mazars R, Gonzalez-de-Peredo A, Cayrol C, Lavigne AC, Vogel JL, Ortega N, Lacroix C, Gautier V, Huet G, Ray A, et al. (2010). The THAP-zinc finger protein THAP1 associates with coactivator HCF-1 and O-GlcNAc transferase: a link between DYT6 and DYT3 dystonias. J Biol Chem 285, 13364–13371. [PubMed: 20200153]

Michaud J, Praz V, James Faresse N, Jnbaptiste CK, Tyagi S, Schutz F, and Herr W (2013). HCFC1 is a common component of active human CpG-island promoters and coincides with ZNF143, THAP11, YY1, and GABP transcription factor occupancy. Genome Res 23, 907–916. [PubMed: 23539139]

Minocha S, Villeneuve D, Praz V, Moret C, Lopes M, Pinatel D, Rib L, Guex N, and Herr W (2019). Rapid Recapitulation of Nonalcoholic Steatohepatitis upon Loss of Host Cell Factor 1 Function in Mouse Hepatocytes. Mol Cell Biol 39.

Mirman Z, and de Lange T (2020). 53BP1: a DSB escort. Genes Dev 34, 7–23. [PubMed: 31896689]

Mirman Z, Lottersberger F, Takai H, Kibe T, Gong Y, Takai K, Bianchi A, Zimmermann M, Durocher D, and de Lange T (2018). 53BP1-RIF1-shieldin counteracts DSB resection through CST- and Polalpha-dependent fill-in. Nature 560, 112–116. [PubMed: 30022158]

Mouse EC, Stamatoyannopoulos JA, Snyder M, Hardison R, Ren B, Gingeras T, Gilbert DM, Groudine M, Bender M, Kaul R, et al. (2012). An encyclopedia of mouse DNA elements (Mouse ENCODE). Genome Biol 13, 418. [PubMed: 22889292]

Nakamura M, Kondo S, Sugai M, Nazarea M, Imamura S, and Honjo T (1996). High frequency class switching of an IgM+ B lymphoma clone CH12F3 to IgA+ cells. Int Immunol 8, 193–201. [PubMed: 8671604]

Nandi S, Liang G, Sindhava V, Angireddy R, Basu A, Banerjee S, Hodawadekar S, Zhang Y, Avadhani NG, Sen R, et al. (2020a). YY1 control of mitochondrial-related genes does not account for regulation of immunoglobulin class switch recombination in mice. Eur J Immunol 50, 822–838. [PubMed: 32092784]

Nandi S, Liang G, Sindhava V, Angireddy R, Basu A, Banerjee S, Hodawadekar S, Zhang Y, Avadhani NG, Sen R, et al. (2020b). YY1 control of mitochondrial-related genes does not account for regulation of immunoglobulin class switch recombination in mice. Eur J Immunol.

Noordermeer SM, Adam S, Setiaputra D, Barazas M, Pettitt SJ, Ling AK, Olivieri M, Alvarez-Quilon A, Moatti N, Zimmermann M, et al. (2018). The shieldin complex mediates 53BP1-dependent DNA repair. Nature 560, 117–121. [PubMed: 30022168]

Ochs F, Karemore G, Miron E, Brown J, Sedlackova H, Rask MB, Lampe M, Buckle V, Schermelleh L, Lukas J, et al. (2019). Stabilization of chromatin topology safeguards genome integrity. Nature 574, 571–574. [PubMed: 31645724]

Ochs F, Somyajit K, Altmeyer M, Rask MB, Lukas J, and Lukas C (2016). 53BP1 fosters fidelity of homology-directed DNA repair. Nat Struct Mol Biol 23, 714–721. [PubMed: 27348077]

Paiano J, Wu W, Yamada S, Sciascia N, Callen E, Paola Cotrim A, Deshpande RA, Maman Y, Day A, Paull TT, et al. (2020). ATM and PRDM9 regulate SPO11-bound recombination intermediates during meiosis. Nat Commun 11, 857. [PubMed: 32051414]

Pannunzio NR, Watanabe G, and Lieber MR (2018). Nonhomologous DNA end-joining for repair of DNA double-strand breaks. J Biol Chem 293, 10512–10523. [PubMed: 29247009]

Petersen S, Casellas R, Reina-San-Martin B, Chen HT, Difilippantonio MJ, Wilson PC, Hanitsch L, Celeste A, Muramatsuk M, Pilch DR, et al. (2001). AID is required to initiate Nbs1/gamma-H2AX focus formation and mutations at sites of class switching. Nature 414, 660–665. [PubMed: 11740565]

Quinlan AR, and Hall IM (2010). BEDTools: a flexible suite of utilities for comparing genomic features. Bioinformatics 26, 841–842. [PubMed: 20110278]

Rooney S, Chaudhuri J, and Alt FW (2004). The role of the non-homologous end-joining pathway in lymphocyte development. Immunol Rev 200, 115–131. [PubMed: 15242400]

Roussigne M, Kossida S, Lavigne AC, Clouaire T, Ecochard V, Glories A, Amalric F, and Girard JP (2003). The THAP domain: a novel protein motif with similarity to the DNA-binding domain of P element transposase. Trends Biochem Sci 28, 66–69. [PubMed: 12575992]

Ruiz M, Perez-Garcia G, Ortiz-Virumbrales M, Meneret A, Morant A, Kottwitz J, Fuchs T, Bonet J, Gonzalez-Alegre P, Hof PR, et al. (2015). Abnormalities of motor function, transcription and cerebellar structure in mouse models of THAP1 dystonia. Hum Mol Genet 24, 7159–7170. [PubMed: 26376866]

Sanjana NE, Shalem O, and Zhang F (2014). Improved vectors and genome-wide libraries for CRISPR screening. Nat Methods 11, 783–784. [PubMed: 25075903]

Scully R, Panday A, Elango R, and Willis NA (2019). DNA double-strand break repair-pathway choice in somatic mammalian cells. Nat Rev Mol Cell Biol 20, 698–714. [PubMed: 31263220]

Setiaputra D, and Durocher D (2019). Shieldin - the protector of DNA ends. EMBO Rep 20.

Shinoda K, Maman Y, Canela A, Schatz DG, Livak F, and Nussenzweig A (2019). Intra-Vkappa Cluster Recombination Shapes the Ig Kappa Locus Repertoire. Cell Rep 29, 4471–4481 e4476. [PubMed: 31875554]

Sigova AA, Abraham BJ, Ji X, Molinie B, Hannett NM, Guo YE, Jangi M, Giallourakis CC, Sharp PA, and Young RA (2015). Transcription factor trapping by RNA in gene regulatory elements. Science 350, 978–981. [PubMed: 26516199]

Stringer BW, Day BW, D'Souza RCJ, Jamieson PR, Ensbey KS, Bruce ZC, Lim YC, Goasdoue K, Offenhauser C, Akgul S, et al. (2019). A reference collection of patient-derived cell line and xenograft models of proneural, classical and mesenchymal glioblastoma. Sci Rep 9, 4902. [PubMed: 30894629]

Tarsounas M, and Sung P (2020). The antitumorigenic roles of BRCA1-BARD1 in DNA repair and replication. Nat Rev Mol Cell Biol 21, 284–299. [PubMed: 32094664]

Tomida J, Takata KI, Bhetawal S, Person MD, Chao HP, Tang DG, and Wood RD (2018). FAM35A associates with REV7 and modulates DNA damage responses of normal and BRCA1-defective cells. EMBO J 37.

Wang B, Wang M, Zhang W, Xiao T, Chen CH, Wu A, Wu F, Traugh N, Wang X, Li Z, et al. (2019). Integrative analysis of pooled CRISPR genetic screens using MAGeCKFlute. Nat Protoc 14, 756–780. [PubMed: 30710114]

Wang L, Zhao H, Li J, Xu Y, Lan Y, Yin W, Liu X, Yu L, Lin S, Du MY, et al. (2020). Identifying functions and prognostic biomarkers of network motifs marked by diverse chromatin states in human cell lines. Oncogene 39, 677–689. [PubMed: 31537905]

Wang Y, Bernhardy AJ, Cruz C, Krais JJ, Nacson J, Nicolas E, Peri S, van der Gulden H, van der Heijden I, O'Brien SW, et al. (2016). The BRCA1-Delta11q Alternative Splice Isoform Bypasses Germline Mutations and Promotes Therapeutic Resistance to PARP Inhibition and Cisplatin. Cancer Res 76, 2778–2790. [PubMed: 27197267]

Ward IM, Minn K, van Deursen J, and Chen J (2003). p53 Binding protein 53BP1 is required for DNA damage responses and tumor suppression in mice. Mol Cell Biol 23, 2556–2563. [PubMed: 12640136]

Ward IM, Reina-San-Martin B, Olaru A, Minn K, Tamada K, Lau JS, Cascalho M, Chen L, Nussenzweig A, Livak F, et al. (2004). 53BP1 is required for class switch recombination. J Cell Biol 165, 459–464. [PubMed: 15159415]

Xu G, Chapman JR, Brandsma I, Yuan J, Mistrik M, Bouwman P, Bartkova J, Gogola E, Warmerdam D, Barazas M, et al. (2015). REV7 counteracts DNA double-strand break resection and affects PARP inhibition. Nature 521, 541–544. [PubMed: 25799992]

Yellajoshyula D, Liang CC, Pappas SS, Penati S, Yang A, Mecano R, Kumaran R, Jou S, Cookson MR, and Dauer WT (2017). The DYT6 Dystonia Protein THAP1 Regulates Myelination within the Oligodendrocyte Lineage. Dev Cell 42, 52–67 e54. [PubMed: 28697333]

Yue F, Cheng Y, Breschi A, Vierstra J, Wu W, Ryba T, Sandstrom R, Ma Z, Davis C, Pope BD, et al. (2014). A comparative encyclopedia of DNA elements in the mouse genome. Nature 515, 355–364. [PubMed: 25409824]

Zakirova Z, Fanutza T, Bonet J, Readhead B, Zhang W, Yi Z, Beauvais G, Zwaka TP, Ozelius LJ, Blitzer RD, et al. (2018). Mutations in THAP1/DYT6 reveal that diverse dystonia genes disrupt similar neuronal pathways and functions. PLoS Genet 14, e1007169. [PubMed: 29364887]

Zhang Y, Liu T, Meyer CA, Eeckhoute J, Johnson DS, Bernstein BE, Nusbaum C, Myers RM, Brown M, Li W, et al. (2008). Model-based analysis of ChIP-Seq (MACS). Genome Biol 9, R137. [PubMed: 18798982]

Zhao W, Wiese C, Kwon Y, Hromas R, and Sung P (2019). The BRCA Tumor Suppressor Network in Chromosome Damage Repair by Homologous Recombination. Annu Rev Biochem 88, 221–245. [PubMed: 30917004]

Zong D, Adam S, Wang Y, Sasanuma H, Callen E, Murga M, Day A, Kruhlak MJ, Wong N, Munro M, et al. (2019). BRCA1 Haploinsufficiency Is Masked by RNF168-Mediated Chromatin Ubiquitylation. Mol Cell 73, 1267–1281 e1267. [PubMed: 30704900]

Highlights:

- Loss of THAP1 rescues homologous recombination in cells lacking BRCA1 but not BRCA2
- A THAP1-YY1-HCF1 transcriptional module drives physiological *SHLD1* expression
- THAP1 promotes NHEJ during immunoglobulin class switching
- Hyperactivation of the THAP1-SHLD1 axis causes genome instability

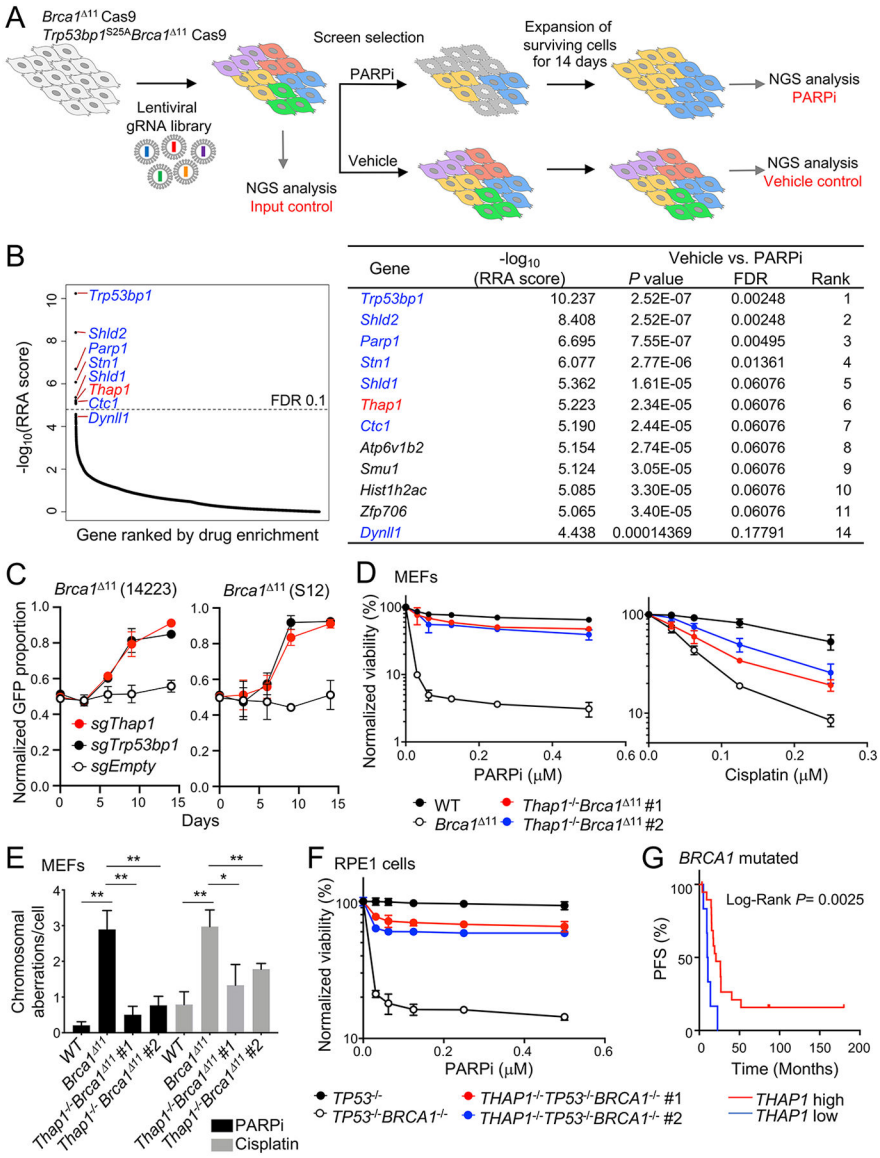

Figure 1. Identification of THAP1 as a modifier of chemosensitivity in BRCA1-deficient cells.

(**A**) Schematic of CRISPR-based screen for genes whose deletion confer resistance to the clinical PARP inhibitor (PARPi) olaparib in *BRCA1*-mutant MEFs (*Brca1*$^{\Delta 11}$ and *Brca1*$^{\Delta 11}$*Trp53bp1*^{S25A}).

(**B**) Analysis of guide RNA enrichment in PARPi survivors by MAGeCK. A false discovery rate (FDR) of 0.1 is indicated by dotted line. The combined top hits for *Brca1*$^{\Delta 11}$ (n=2) and *Brca1*$^{\Delta 11}$*Trp53bp1*^{S25A} (n=1) screens are tabulated on the right: summary of n = 3 biological replicates. Previously identified resistance genes are shown in blue and *Thap1* is shown in red.

(**C**) Multicolor Competition Assay (MCA): *Cas9*$^{+}$ *Brca1*$^{\Delta 11}$ MEFs (14223 and S12) transduced with a specific guide RNA targeting *Thap1*, *Trp53bp1* or an empty vector (sgEmpty, all GFP-positive) were co-incubated (1:1 ratio) with *Cas9*$^{+}$ *Brca1*$^{\Delta 11}$ MEFs transduced with non-targeting guides (sgLacZ, mCherry-positive). Data represent mean

fraction of GFP-positive cells ± s.d., normalized to day 0 (n = 3). Deletion of *Thap1* significantly enhanced the outgrowth of *Brca1*$^{\Delta 11}$ cells following PARPi (100 nM) treatment ($p<0.0001$).

(**D**) Viability of *WT*, *Brca1*$^{\Delta 11}$ (14223) and two individual clones (#1 and #2) of *Thap1*$^{-/-}$ *Brca1*$^{\Delta 11}$ MEFs (derived from 14223), as measured by CellTiter-Glo seven days after treatment with PARPi (left) and cisplatin (right).

(**E**) Genomic instability detected in the metaphase spreads of *WT*, *Brca1*$^{\Delta 11}$ and two individual clones (#1 and #2) of *Thap1*$^{-/-}$*Brca1*$^{\Delta 11}$ MEFs. Cells were treated for 16 h with 1 μM PARPi or with 0.5 μM cisplatin. At least 50 metaphase spreads were scored per genotype and condition. The experiments were repeated four (PARPi) and three (cisplatin) times, respectively. Statistical significance was determined by Welch's t-test. Representative metaphase spreads are shown in Figure S1C.

(**F**) Viability of *TP53*$^{-/-}$, *TP53*$^{-/-}$*BRCA1*$^{-/-}$ and two individual clones (#1 and #2) of *THAP1*$^{-/-}$*TP53*$^{-/-}$*BRCA1*$^{-/-}$ human RPE1 cells, as measured by CellTiter-Glo seven days after PARPi treatment.

(**G**) Progression-free survival (PFS) of BRCA1-mutated ovarian serous adenocarcinoma patients with standard platinum-based regimens (Cancer Genome Atlas Research, 2011). Patients were defined as having *THAP1* low- (n=7) or high-expressing (n=22) tumors on the basis of the quintile of *THAP1* expression (z-scores < −0.67). PFS curves were generated by the Kaplan–Meier method. The difference between the PFS of *THAP1* low-versus *THAP1* high-expressing patients was assessed by the log-rank test ($P < 0.01$). See also Figures S1.

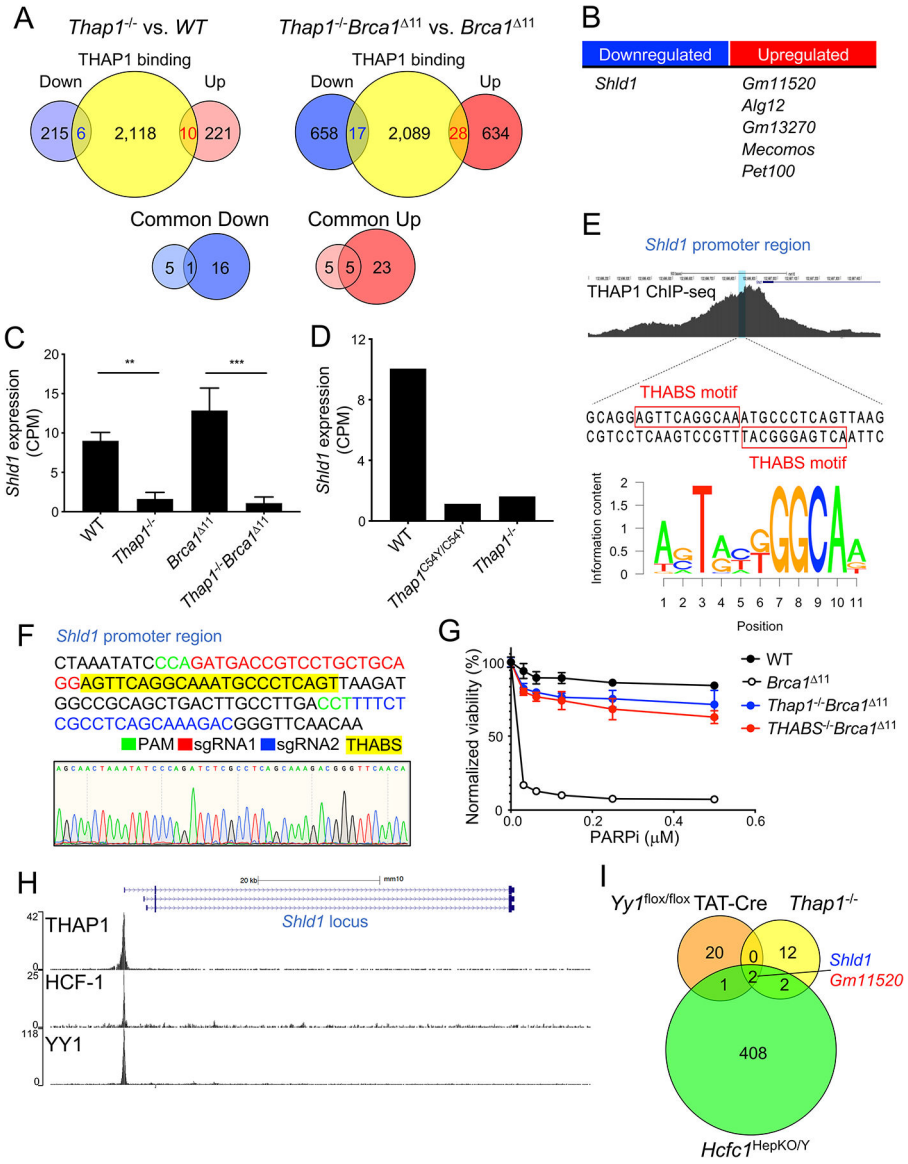

Figure 2. THAP1 co-regulates *Shld1* expression with HCF1 and YY1.

(**A**) Top: Venn diagram depicting differentially expressed genes (nascent RNA-seq, log2 fold-change >2 and FDR <0.05) in *Thap1*$^{-/-}$ versus *WT* and *Thap1*$^{-/-}$*Brca1*$^{\Delta 11}$ versus *Brca1*$^{\Delta 11}$ MEFs in relation to THAP1-bound genes (ChIP-seq). The number of genes that were shown to be bound by THAP1 and were either downregulated or upregulated in THAP1-deficient MEFs are shown in blue and red, respectively.

Bottom: Venn diagram showing the number of differentially expressed THAP1-bound genes that were common to both *Thap1*$^{-/-}$ and *Thap1*$^{-/-}$*Brca1*$^{\Delta 11}$ MEFs.

(**B**) List of differentially expressed THAP1-bound genes that were common to both *Thap1*$^{-/-}$ and *Thap1*$^{-/-}$*Brca1*$^{\Delta 11}$ MEFs.

(**C**) Levels of *Shld1* gene expression in *WT, Thap1*$^{-/-}$*, Brca1*$^{\Delta 11}$ and *Thap1*$^{-/-}$*Brca1*$^{\Delta 11}$ MEFs, as detected by nascent RNA-seq. Data represent mean counts per million reads

(CPM) ± s.d. (n = 3, **p<0.01, ***p<0.001). Statistical significance were determined by one-way ANOVA.

(**D**) Levels of *Shld1* gene expression in *WT, Thap*$^{C54Y/C54Y}$ *and Thap1*$^{-/-}$ mESCs. Data are from a publicly available RNA-seq dataset (GSE86911). Data represent mean CPM.

(**E**) Top: The location of the THAP1 binding sequence (THABS) motif within the *Shld1* promoter. THAP1 ChIP-seq signal at the Shld1 promoter region is shown above. Bottom: The 11-nucleotide consensus DNA-binding sequence recognized by the THAP domain of THAP1.

(**F**) Top: Genomic sequences within mouse *Shld1* promoter region is shown. Two independent sgRNAs used to delete THABS sequence (sgRNA1; red and sgRNA2; blue) are shown along with their respective PAM sequences (green).

Bottom: Confirmation of successful editing of the *THABS*$^{-/-}$ MEF clone is shown.

(**G**) Viability of *WT*, *Brca1*$^{\Delta 11}$, *Thap1*$^{-/-}$*Brca1*$^{\Delta 11}$ and *THABS*$^{-/-}$*Brca1*$^{\Delta 11}$ MEFs were measured by CellTiter-Glo seven days after PARPi treatment.

(**H**) Binding of THAP1, HCF1 and YY1 at the *Shld1* gene locus. Data are from publicly available ChIP-seq datasets in ES cells (THAP1, GSE86911; HCF1, GSE36030; YY1, GSE68195).

(**I**) Venn diagram depicting differentially expressed genes (log2 fold-change >2 and FDR <0.05) in *Thap1*$^{-/-}$ MEFs, *Yy1*$^{flox/flox}$ TAT-Cre mouse B cells, and *Hcfc1*$^{HepKO/Y}$ hepatocytes in relation to THAP1-bound genes and previously published YY1- and HCF1-bound genes. Only two genes bound by all three transcription factors also exhibited differential expression: *Shld1* (downregulated) and *Gm11520* (upregulated). See also Figure S2.

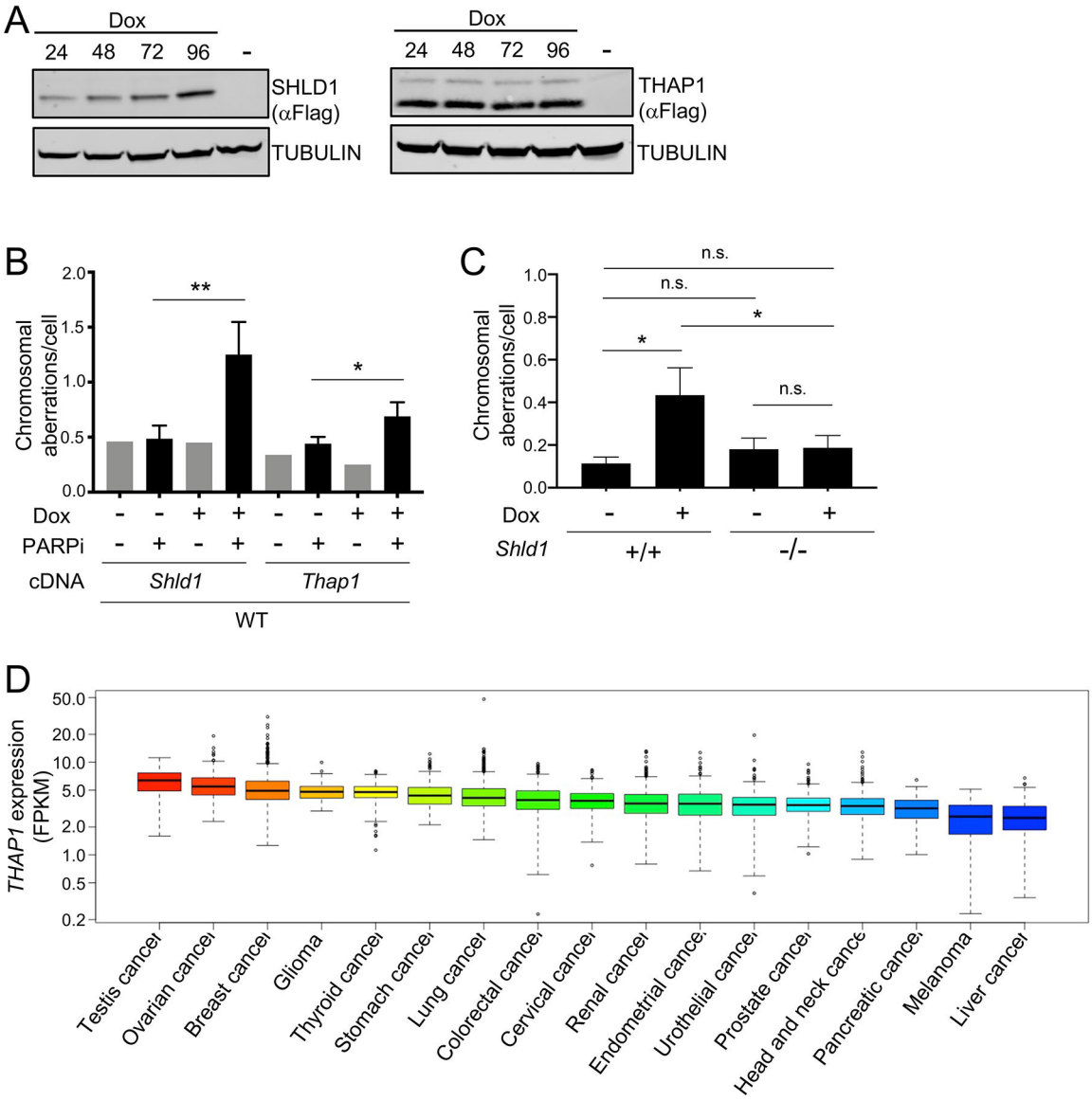

Figure 3. Imbalances in the THAP1-SHLD1 axis threaten genome stability.

(**A**) Western blot analysis of doxycycline-dependent expression of exogenous SHLD1 (left) and THAP1 (right) proteins in *WT* MEFs 24 to 96 hours after induction with doxycycline (Dox) as detected by anti-Flag antibody.

(**B**) Genomic instability detected in the metaphase spreads of *WT* MEFs overexpressing SHLD1 or THAP1 with or without 16 h of PARPi treatment (1 μM). Ectopic SHLD1 and THAP1 expression was induced by Dox treatment. At least 50 cells were scored per genotype and condition. The experiments were repeated four times for PARPi treated condition and twice for untreated condition. Statistical significance was determined by Welch's t-test. Representative metaphase spreads are shown in Figure S3A.

(**C**) Endogenous *Shld1* gene was knocked out by CRISPR/Cas9 in *WT* MEFs harboring a Dox-inducible THAP1 overexpression construct. After Dox was added to induce THAP1, cells were treated with PARPi and chromosomal aberrations were examined in

metaphase spreads. SHLD1-proficient cells served as controls. At least 50 cells were scored per genotype and condition. The experiments were repeated three times and statistical significance was determined by Welch's t-test. Representative metaphase spreads are shown in Figure S3B.

(**D**) Expression of the *THAP1* gene (FPKM) in 17 different cancer types. Data were obtained from The Cancer Genome Atlas (TCGA) project. See also Figure S3.

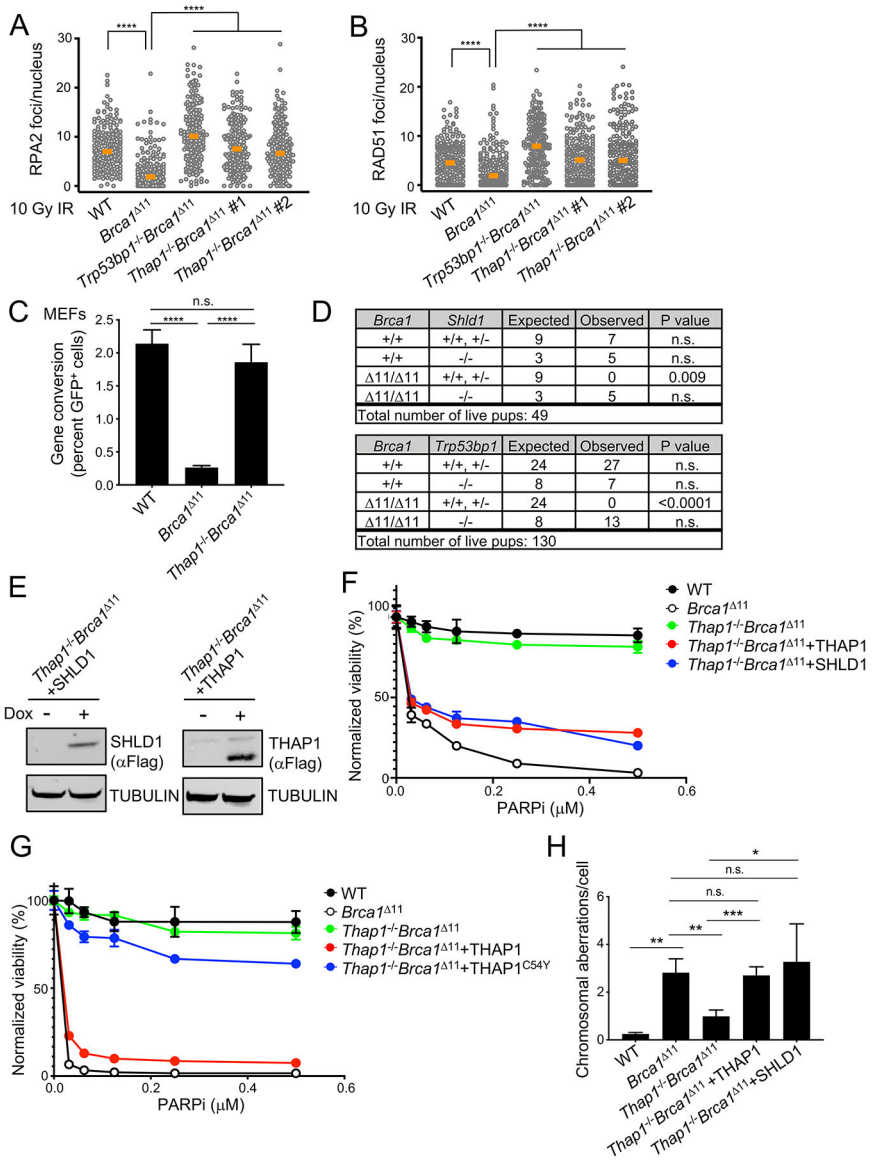

Figure 4. THAP1-dependent *Shld1* expression inhibits HR and drives PARPi hypersensitivity in BRCA1-deficient cells.

(**A-B**) Quantification of RPA2 (**A**) and RAD51 (**B**) foci in individual EdU-positive (S-phase) nuclei of *WT, Brca1*$^{\Delta 11}$*, Trp53bp1*$^{-/-}$*Brca1*$^{\Delta 11}$ and two individual clones of *Thap1*$^{-/-}$*Brca1*$^{\Delta 11}$ MEFs. Cells were irradiated with 10 Gy and analyzed 4 h post-IR. Statistical significance was determined by Welch's t-test.

(**C**) *WT*, *Brca1*$^{\Delta 11}$, and *Thap1*$^{-/-}$*Brca1*$^{\Delta 11}$ MEFs expressing the Traffic Light reporter construct were nucleofected with BFP-tagged I-SceI expressing vector. GFP fluorescent among BFP-positive cells were analyzed by flow cytometry. Bars represent the mean ± s.d..

(**D**) Summary of breeding outcomes from the *Brca1*$^{+/\Delta 11}$*Shld1*$^{+/-}$ × *Brca1*$^{+/\Delta 11}$*Shld1*$^{+/-}$ intercross (Top), and the *Brca1*$^{+/\Delta 11}$*Trp53bp1*$^{+/-}$ x *Brca1*$^{+/\Delta 11}$*Trp53bp1*$^{+/-}$ intercross (Bottom).

(**E**) Western blot analysis of doxycycline-dependent expression of exogenous SHLD1 and THAP1 proteins in *Thap1*$^{-/-}$ *Brca1*$^{\Delta 11}$ MEFs 96 hours (SHLD1) and 72 hours (THAP1) after induction with doxycycline (Dox), as detected by anti-Flag antibody.
(**F-G**) Viability of *WT*, *Brca1*$^{\Delta 11}$, *Thap1*$^{-/-}$*Brca1*$^{\Delta 11}$ and *Thap1*$^{-/-}$*Brca1*$^{\Delta 11}$ MEFs complemented with either THAP1 (*Thap1*$^{-/-}$*Brca1*$^{\Delta 11}$+THAP1), SHLD1 (*Thap1*$^{-/-}$*Brca1*$^{\Delta 11}$+SHLD1) (**F**) or THAP1^{C54Y} (*Thap1*$^{-/-}$*Brca1*$^{\Delta 11}$+THAP1^{C54Y}) (**G**) cDNA, as measured by CellTiter-Glo seven days after PARPi treatment.
(**H**) Genomic instability detected in the metaphase spreads of *WT*, *Brca1*$^{\Delta 11}$, *Thap1*$^{-/-}$*Brca1*$^{\Delta 11}$, *Thap1*$^{-/-}$*Brca1*$^{\Delta 11}$+THAP1, and *Thap1*$^{-/-}$*Brca1*$^{\Delta 11}$+SHLD1 MEFs after 16 h of PARPi treatment (1 μM). At least 50 cells were scored per genotype. Representative metaphase spreads are shown in Figure S5D. The experiment was repeated five times. Statistical significance was determined by Welch's t-test. See also Figures S4 and S5.

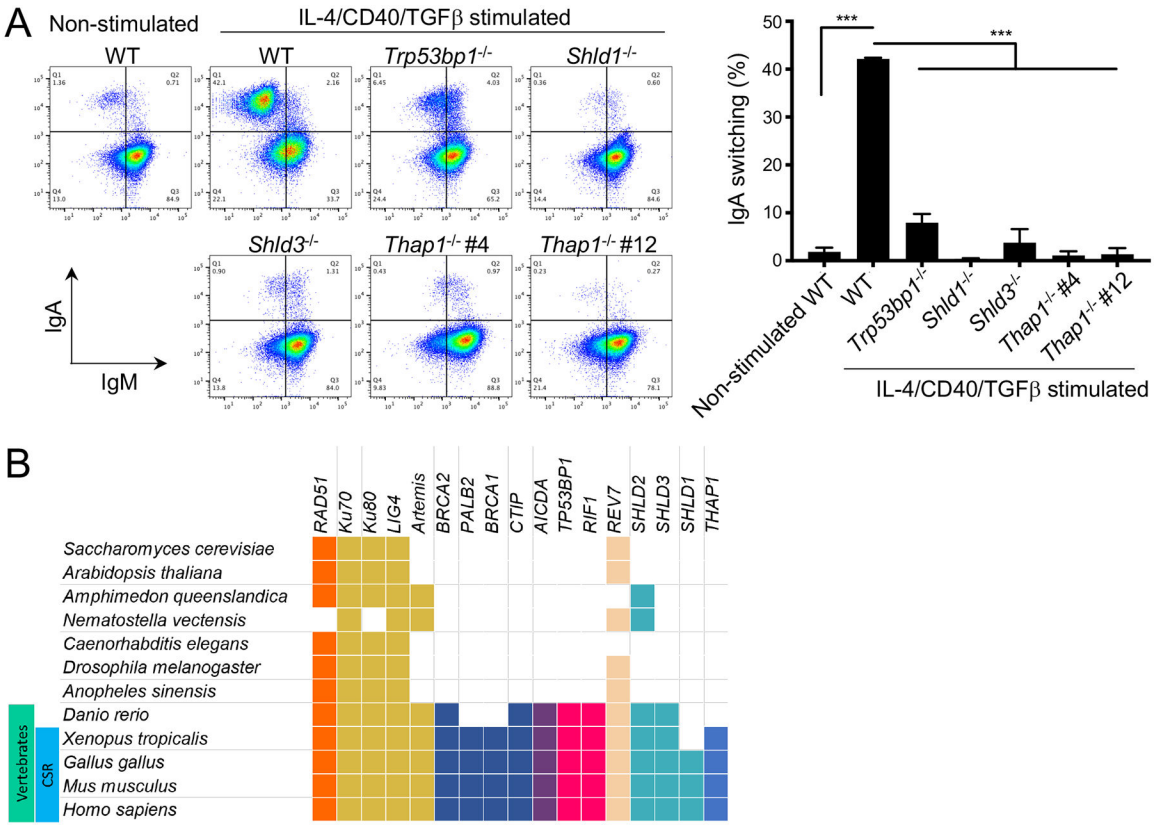

Figure 5. THAP1 participates in physiological NHEJ.

(**A**) Representative flow cytometry plots of IgM-to-IgA class switch recombination (CSR) in *WT*, *Trp53bp1*$^{-/-}$, *Shld1*$^{-/-}$, *Shld3*$^{-/-}$ and two individual clones of *Thap1*$^{-/-}$ (#4 and #12) CH12-F3 cells 24 hours after cytokine stimulation (IL-4, CD40L and TGFβ). Unstimulated WT cells are shown as a negative control. Quantification of IgM-to-IgA CSR is shown on the right and represents mean ± s.d., n=3.

(**B**) Presence/absence table of selected genes in representative organisms, based on orthology data from the Ensembl database. Genes encoding THAP1, the Shieldin components and additional DSB repair factors are shown in relation to antibody CSR.

KEY RESOURCES TABLE

REAGENT or RESOURCE	SOURCE	IDENTIFIER
Antibodies		
Rabbit polyclonal anti-53BP1	Novus Biologicals	Cat# NB100-305; RRID: AB_10001695
Rabbit polyclonal anti-RPA32/RPA2 (pS4, S8)	Novus Biologicals	Cat# NBP1-23017; RRID: AB_1726226
Rat monoclonal anti-RPA32/RPA2 (4E4)	Cell Signaling Technology	Cat# 2208; RRID: AB_2238543
Mouse monoclonal anti-FLAG (M2)	Sigma-Aldrich	Cat# F1804; RRID: AB_262044
Mouse monoclonal anti-α-Tubulin	Sigma-Aldrich	Cat# T-5168; RRID: AB_477579
Rabbit polyclonal anti-RAD51	Abcam	Cat# ab176458; RRID: AB_2665405
Rabbit polyclonal anti-RIF1	Gift from Davide Robbiani	N/A
Mouse monoclonal anti-GFP	Roche Applied Science	Cat# 11814460001; RRID: AB_390913
IRDye 680RD Goat anti-Mouse IgG (H+L)	LI-COR Biosciences	Cat# 925-68070; RRID: AB_2651128
IRDye 800CW Goat anti-Mouse IgG (H+L)	LI-COR Biosciences	Cat# 926-32210; RRID: AB_621842
IRDye 680RD Goat anti-Rabbit IgG (H+L)	LI-COR Biosciences	Cat# 925-68071; RRID: AB_2721181
IRDye 800CW Goat anti-Rabbit IgG (H+L)	LI-COR Biosciences	Cat# 925-32211; RRID: AB_2651127
Alexa Fluor 488 Goat anti-Mouse IgG (H+L)	Thermo Fisher Scientific	Cat# A11001; RRID: AB_2534069
Alexa Fluor 568 Goat anti-Mouse IgG (H+L)	Thermo Fisher Scientific	Cat# A11031; RRID: AB_144696
Alexa Fluor 568 Goat anti-Rat IgG (H+L)	Thermo Fisher Scientific	Cat# A11077; RRID: AB_2534121
Alexa Fluor 488 Chicken anti-Rabbit IgG (H+L)	Thermo Fisher Scientific	Cat# A21441; RRID: AB_10563745
Alexa Fluor 568 Goat anti-Rabbit IgG (H+L)	Thermo Fisher Scientific	Cat# A11011; RRID: AB_143157
Purified Rat anti-Mouse CD180 (RP/14)	BD Biosciences	Cat# 552128; RRID: AB_394343
Purified Rat anti-Mouse CD16/CD32 (2.4G2) Fc Block™	BD Biosciences	Cat# 553141; RRID: AB_394656
Biotin Rat anti-Mouse IgG1 (A85-1)	BD Biosciences	Cat# 553441; RRID: AB_394861
PE Rat anti-Mouse B220 (RA3-6B2)	BD Biosciences	Cat# 553088; RRID: AB_10893353
Purified Rat anti-Mouse CD180 (RP/14)	BD Biosciences	Cat# 552128; RRID: AB_394343
IgM Monoclonal Antibody (II/41), FITC	Thermo Fisher Scientific	Cat# 11-5790-81; RRID: AB_465244
Goat anti-Mouse IgA-PE	Southern Biotech	Cat# 1040-09; RRID: AB_2794375
Bacterial and Virus Strains		
Bacteria: TOP10 Chemically Competent *E. coli*	Thermo Fisher Scientific	Cat# C404006
Bacteria: STBL3 Chemically Competent *E. coli*	Thermo Fisher Scientific	Cat# C737303
Lentivirus: pRSV-Rev	(Dull et al., 1998)	Cat# 12253; RRID: Addgene_12253

REAGENT or RESOURCE	SOURCE	IDENTIFIER
Lentivirus: pMDLg/pRRE	(Dull et al., 1998)	Cat# 12251; RRID: Addgene_12251
Lentivirus: pHCMVG	ATCC	Cat# 75497
Lentivirus: lentiCas9-Blast	(Sanjana et al., 2014)	Cat# 52962; RRID: Addgene_52962
Lentivirus: lentiCRISPRv2	(Sanjana et al., 2014)	Cat# 52961; RRID: Addgene_52961
Lentivirus: lentiCRISPRv2 neo	(Stringer et al., 2019)	Cat# 98292; RRID: Addgene_98292
Lentivirus: pCW-eGFP-SHLD3	(Noordermeer et al., 2018)	Cat# 114126; RRID: Addgene_114126
Lentivirus: pLentiGuide-puro GFP-NLS	Gift from Daniel Durocher	N/A
Lentivirus: pLentiGuide-puro mCherry-NLS	Gift from Daniel Durocher	N/A
Mammalian expression: SP-Cas9	(D'Astolfo et al., 2015)	Cat# 62731; RRID: Addgene_62731
Mammalian expression: pX330-U6-Chimeric_BB-CBh-hSpCas9	(Cong et al., 2013)	Cat# 42230; RRID: Addgene_42230
Mammalian expression: pcDNA3.1-Hygro-delta-hCD4	Gift from Eugene Oltz	N/A
Mammalian expression: PB-TRE-dCas9-VPR	(Chavez et al., 2015)	Cat# 63800; RRID: Addgene_63800
Mammalian expression: PB-TRE-mTHAP1	This paper	N/A
Mammalian expression: PB-TRE-mSHLD1	This paper	N/A
Mammalian expression: PB-TRE- mTHAP1^{C54Y}	This paper	N/A
Lentivirus: pCVL.SFFV.d14GFP.EF1a.HA.NLS.Sce(opt).T2A.TagBFP	Gift from Andrew Scharenberg	Cat# 32627; RRID: Addgene_32627
Lentivirus: pCVL Traffic Light Reporter 1.1 (Sce target) Ef1a Puro	(Certo et al., 2011)	Cat# 31482; RRID: Addgene_31482
Mammalian expression: pCMV-SV40T	Gift from Kai Ge	N/A
Mouse CRISPR Knockout Pooled Library (Brie)	(Doench et al., 2016)	Cat# 73632; RRID: Addgene_73632
Chemicals, Peptides, and Recombinant Proteins		
Olaparib	Selleckchem	Cat# AZD2281
Cisplatin	Sigma-Aldrich	Cat# 479306
Lipopolysaccharide (LPS) from *E. coli* O111:B4	Sigma-Aldrich	Cat# L2630
Interleukin 4 (IL-4) from mouse	Sigma-Aldrich	Cat# I1020
CD43 microbeads (Ly-48)	Miltenyi Biotec	Cat# 130-049-801
X-tremeGENE™ 9 DNA Transfection Reagent	Roche Diagnostics	Cat# 6365809001
Gibson Assembly Cloning Kit	NEB	Cat# E5510S
Zero Blunt™ PCR Cloning Kit	Thermo Fisher Scientific	Cat# K270020
PNA probe for telomeres Cy3-$(CCCTAA)_3$	PNA Bio	Cat# F1002
DAPI	Thermo Fisher Scientific	Cat# 62248
EdU	Thermo Fisher Scientific	Cat# A10044
Colcemid	Roche Diagnostics	Cat# 10295892001
Dynabeads Protein A	Thermo Fisher Scientific	Cat# 10002D

REAGENT or RESOURCE	SOURCE	IDENTIFIER
cOmplete, Mini Protease inhibitor cocktail	Roche Diagnostics	Cat# 11836153001
Puregene Proteinase K enzyme	Qiagen	Cat# 158920
Puregene RNase A Solution	Qiagen	Cat# 158924
T4 DNA Polymerase	NEB	Cat# M0203L
T4 Polynucleotide Kinase	NEB	Cat# M0201L
DNA Polymerase I, Large (Klenow) Fragment	NEB	Cat# M0210L
Exonuclease T (ExoT)	NEB	Cat# M0265L
Klenow Fragment (3′→5′ exo-)	NEB	Cat# M0212L
Quick Ligation Kit	NEB	Cat# M2200L
KAPA HiFi HotStart ReadyMix (2X)	KAPA Biosystems	Cat# KK2600
MyOne Streptavidin C1 Beads	ThermoFisher	Cat# 650-01
Agencourt AMPure XP beads	Beckman Coulter	Cat# A63881
Phusion High-Fidelity PCR Master Mix with HF buffer	NEB	Cat# M0531L
Recombinant Human TGF-beta 1 Protein	R&D	Cat# 240-B
Recombinant Murine sCD40 Lignad	PeproTech	Cat# 315-15
TRIzol	Thermo Fisher Scientific	Cat# 15596018
MyTaq™ Red Mix	Bioline	Cat# BIO-25044
Critical Commercial Assays		
KAPA Library Quantification Kit	Kapa Biosciences	Cat# KK4824
EasySep Human CD4 Positive Selection Kit II	STEMCELL technologies	Cat# 18052
Click-IT EdU Alexa Fluor 488 Flow Cytometry Assay Kit	Thermo Fisher Scientific	Cat# C10425
Click-IT EdU Alexa Fluor 647 Flow Cytometry Assay Kit	Thermo Fisher Scientific	Cat# C10634
Geneticin™ Selective Antibiotic (G418 Sulfate)	Thermo Fisher Scientific	Cat# 10131027
CellTiter-Glo® Luminescent Cell Viability Assay	Promega	Cat# G7571
ESGRO® Recombinant Mouse LIF Protein	Sigma-Aldrich	Cat# ESG1107
Fetal Bovine Serum, embryonic stem cell-qualified	Thermo Fisher Scientific	Cat# 16141079
iSCRIPT Advanced cDNA Synthesis Kit	Bio-Rad	Cat# 1725037
SsoAdvanced™ Universal SYBR Green Supermix	Bio-Rad	Cat# 1725271
Mouse Embryonic Fibroblast Nucleofector™ Kit 2	Lonza	Cat# VVPD-1005
PrimePCR™ SYBR Green Assay: Actb, Mouse	Bio-Rad	Cat# qMmuCED0027505
PrimePCR™ SYBR Green Assay: 1110034G24Rik, Mouse	Bio-Rad	Cat# qMmuCID0014233
Blood & Cell Culture DNA Midi Kit	QIAGEN	Cat# 13343
ChIP DNA Clean & Concentrator	Zymo Research	Cat# D5205
Deposited Data		
Raw and analyzed data	This paper	GSE154729
RNA-seq and ChIP-seq datasets for *Thap1*$^{-/-}$ in mESC	(Aguilo et al., 2017)	GSE86911
RNA-seq and ChIP-seq datasets for *Yy1*$^{flox/flox}$ TAT-Cre in primary B cells	(Nandi et al., 2020a)	GSE145161
ChIP-seq dataset for YY1 in mESC	(Sigova et al., 2015)	GSE68195
ChIP-seq dataset for HCF1 in mESC	(Mouse et al., 2012)	GSE36030

REAGENT or RESOURCE	SOURCE	IDENTIFIER
ChIP-seq dataset for THAP1 in K562 cells	(Gertz et al., 2013)	GSE32465
ChIP-seq dataset for HCF1 and YY1 in K562 cells	(Consortium, 2012)	GSE31477
Unprocessed images	This paper	http://dx.doi.org/10.17632/35jfgtzkk4.1
Experimental Models: Cell Lines		
MEF: Wildtype	(Callen et al., 2020)	N/A
MEF: *Brca1* $^{\Delta 11/\Delta 11}$	(Callen et al., 2020)	N/A
MEF: *Thap1*$^{-/-}$*Brca1* $^{\Delta 11/\Delta 11}$ Clone 1	This paper	N/A
MEF: *Thap1*$^{-/-}$*Brca1* $^{\Delta 11/\Delta 11}$ Clone 2	This paper	N/A
MEF: *Thap1*$^{-/-}$*Brca1* $^{\Delta 11/\Delta 11}$ inducible THAP1	This paper	N/A
MEF: *Thap1*$^{-/-}$*Brca1* $^{\Delta 11/\Delta 11}$ inducible THAP1^{C54Y}	This paper	N/A
MEF: *Thap1*$^{-/-}$*Brca1* $^{\Delta 11/\Delta 11}$ inducible SHLD1	This paper	N/A
MEF: Wildtype inducible THAP1	This paper	N/A
MEF: Wildtype inducible SHLD1	This paper	N/A
MEF: *Shld1*$^{-/-}$ inducible THAP1	This paper	N/A
hTERT-RPE1: *BRCA1*$^{-/-}$ *p53*$^{-/-}$	This paper	N/A
hTERT-RPE1: *THAP1*$^{-/-}$*BRCA1*$^{-/-}$ *p53*$^{-/-}$ clone 1	This paper	N/A
hTERT-RPE1: *THAP1*$^{-/-}$*BRCA1*$^{-/-}$ *p53*$^{-/-}$ clone 2	This paper	N/A
mES: *Brca2*^{Y3308X}	(Kuznetsov et al., 2008)	N/A
mES: *Thap1*$^{-/-}$*Brca2*^{Y3308X}	This paper	N/A
Mouse B cell: CH12-F3	(Nakamura et al., 1996)	N/A
Mouse B cell: CH12-F3 *Trp53bp1*$^{-/-}$	(Gupta et al., 2018)	N/A
Mouse B cell: CH12-F3 *Shld1*$^{-/-}$	(Gupta et al., 2018)	N/A
Mouse B cell: CH12-F3 *Shld3*$^{-/-}$	(Gupta et al., 2018)	N/A
Mouse B cell: CH12-F3 *Thap1*$^{-/-}$ #4	This paper	N/A
Mouse B cell: CH12-F3 *Thap1*$^{-/-}$ #12	This paper	N/A
Experimental Models: Organisms/Strains		
Mouse: BRCA1$^{+/\Delta 11}$. B6/129	NCI mouse repository	Strain # 01XC9
Mouse: BRCA1$^{F\Delta 11/F\Delta 11}$CD19Cre. B6/129	NCI mouse repository	Strain # 01XC8
Mouse: 53BP1$^{-/-}$. B6/129	(Ward et al., 2003)	N/A
Mouse: SHLD1$^{-/-}$. B6/129	This paper	N/A
Oligonucleotides		
sgRNA to generate mouse Thap1$^{-/-}$ cells, see Table S3	This paper	N/A
sgRNA to generate mouse Shld1$^{-/-}$ cells, see Table S3	This paper	N/A
sgRNA to generate human THAP1$^{-/-}$ cells, see Table S3	This paper	N/A
Primers used for sgRNA target site mutation in mouse Thap1, see Table S3	This paper	N/A
Primers used for generation of THAP1^{C54Y} mutation, see Table S3	This paper	N/A
sgRNA to generate THABS$^{-/-}$ cells, see Table S3	This paper	N/A

REAGENT or RESOURCE	SOURCE	IDENTIFIER
sgRNA used for generation of Shld1$^{-/-}$ mouse, see Table S3	This paper	N/A
Primers used for genotyping of Shld1$^{-/-}$ mouse, see Table S3	This paper	N/A
Primers used for PCR of sgRNA for illumina sequencing, see Table S3	(Doench et al., 2016)	N/A
Software and Algorithms		
ZEN 2 (blue edition)	Zeiss	https://www.zeiss.com/
Metafer 4	MetaSystems	https://metasystems-international.com/
Prism 8	GraphPad	https://www.graphpad.com/
ImageJ	National Institutes of Health	https://imagej.nih.gov/ij
RStudio	RStudio Team	https://www.rstudio.com/
FlowJo (10.1)	FlowJo LLC	https://www.flowjo.com/
Bowtie 1.1.2	(Langmead et al., 2009)	https://sourceforge.net/projects/bowtie-bio/files/bowtie/1.1.2/
MACS 1.4.3	(Zhang et al., 2008)	https://pypi.org/pypi/MACS/1.4.3
UCSC database	(Karolchik et al., 2004)	https://genome.ucsc.edu
UCSC genome browser	(Kent et al., 2002)	https://genome.ucsc.edu
Bedtools	(Quinlan and Hall, 2010)	https://github.com/arq5x/bedtools2
R 3.6.1	R Core Team	https://www.r-project.org/
MAGeCK software package version 0.5.9.2	(Wang et al., 2019)	https://sourceforge.net/projects/mageck/files/0.5/
Other		
293T lentivirus packaging cells	ATCC	Cat# CRL-11268; RRID: CVCL_1926
P19 mouse cells	ATCC	Cat# CRL-1825; RRID: CVCL_2153
Glass Bottom Microwell Dishes	MatTek Corporation	Cat# P35G-1.5-14-C
Axio Observer Z1 epifluorescence microscope	Zeiss	N/A
IN Cell Analyzer	GE Healthcare	N/A
Odyssey® CLx Imaging System	LI-COR Biosciences	N/A
FACSCalibur	BD Biosciences	N/A
Nano Quant Infinite M200 Pro microplate reader	Tecan	N/A
Mark 1 ^{137}Cs irradiator	JL Shepherd	N/A
Cytogenetic drying chamber	Thermotron	N/A
CFX96 Real-Time System	Bio-Rad	N/A
Amaxa Nucleofector IIb	Lonza	N/A
FACSAria II cell sorter	BD Biosciences	N/A
FACSCanto II	BD Biosciences	N/A
Lion heart LX automated microscope	BioTek	N/A